Numerical modeling of bioinspired tri-layer scaffolds for heart valve constructs

by

Yueen Liu

A thesis
submitted to the University of Ottawa
in partial fulfillment of the
thesis requirement for the degree of
Master of Applied Science
in
Mechanical Engineering

Ottawa, Ontario, Canada, 2025

Examining committee

The following served on the Examining Committee for this thesis.

External Examiner:	Rong Liu, Professor Department of Mechanical and Aerospace Engineering Carleton University
Internal Member:	James McDonald, Associate Professor Department of Mechanical Engineering University of Ottawa
Supervisor:	Tao Jin, Assistant Professor Department of Mechanical Engineering University of Ottawa

Declaration of authorship

I hereby certify that this thesis is entirely my own original work except where otherwise indicated. I am aware of the University's regulations concerning plagiarism, including those concerning consequent disciplinary actions. Any use of the works of any other author, in any form, is properly acknowledged at their point of use.

Abstract

For many patients suffering from heart valve diseases, heart valve replacement surgery is the primary treatment option. Currently, there are two types of artificial valves clinically available for the replacement surgery, the mechanical valve and the bioprosthetic valve. The former is typically made from durable materials and can last for a long time. However, lifelong medical treatment with blood thinner is required to reduce the clot risk. The latter is generally made from animal valves and could avoid the long-term use of medication. However, it suffers from biocompatibility issues and relatively short service life due to calcification. With the recent advancement in tissue engineering, tissue-engineered heart valves provide a promising potential to overcome the limitations of the existing artificial heart valves. Among various fabrication methods, the electrospinning technology offers an effective approach to fabricate scaffold materials needed in the artificial heart valve. In order to ensure that the fabricated scaffold material mimics the mechanical properties of native valve tissues, solely relying on experimental trial-and-error is labor-intensive, time-consuming, and financially expensive. On the other hand, numerical methods, especially finite element simulations, provide an efficient approach to investigate the mechanical properties of fabricated scaffold materials. In this thesis, a computational framework based on the finite element method is developed to model the mechanical responses of the bioinspired tri-layer scaffold used for heart valve constructs. This scaffold material is composed of a top layer and a bottom layer containing mutually orthogonal fiber alignments as well as a middle layer possessing a honeycomb pattern. A hyperelastic material constitutive model is developed as the material constitutive model, and a three-field mixed finite element approach is adopted to enforce the material incompressibility. The details of the developed numerical technique are presented, including the material constitutive formulation and the finite element approach in the framework of the nonlinear solid mechanics. The obtained numerical results are compared with the experimental observations, and the detailed stress distributions among various scaffold layers are revealed. The force-displacement relationship confirms that the fabricated tri-layer scaffold exhibits similar mechanical properties as native heart valve tissues.

Acknowledgements

The experimental data used in this work is provided by the research team of Dr. Xing Zhang at the Chinese Academy of Sciences. Their expertise and suggestions are greatly appreciated. This work is partially supported by the Natural Sciences and Engineering Research Council of Canada (NSERC) under the Discovery Grants Program (funding reference number: RGPIN-2021-02561, principle investigator: Tao Jin, PhD). Their financial support is greatly appreciated.

Dedication

I would like to dedicate this work to my parents. Their unwavering support and trust in me have always been my greatest motivation. I am also deeply grateful to my supervisor, Professor Tao Jin, for his valuable guidance throughout this study.

Table of Contents

List of Tables

List of Figures

List of Symbols

$\mathbf{F}$	deformation gradient
$\boldsymbol{x}$	coordinate in the current (deformed) configuration
$\boldsymbol{X}$	coordinate in the initial (reference) configuration
$\mathbf{C}$	right Cauchy-Green deformation tensor
$\mathbf{b}$	left Cauchy-Green deformation tensor
$\mathbf{E}$	Lagrangian-Green strain tensor
$\mathbf{e}$	Eulerian (Almansi) strain tensor
$\mathbf{R}$	rotation tensor
$\mathbf{U}$	stretch tensor in reference configuration
$\mathbf{V}$	stretch tensor in deformed configuration
$\bar{\mathbf{F}}$	distortional component of the deformation gradient
J	determinant of the deformation gradient
$\boldsymbol{\sigma}$	Cauchy stress
$\boldsymbol{\tau}$	Kirchhoff stress
$\mathbf{P}$	1st Piola-Kirchhoff stress
$\mathbf{S}$	2nd Piola-Kirchhoff stress
Ψ	elastic strain energy
$\mathbf{c}$	spatial elasticity tensor
$\mathbb{C}$	material elasticity tensor
I_1	first principal tensor invariant
I_2	second principal tensor invariant
I_3	third principal tensor invariant
K	bulk modulus
G	shear modulus
ν	Poisson's ratio
p	pressure
I_4	pseudo invariant

$\mathbf{A}$	structural tensor
$\mathbf{I}$	2nd-order identity tensor
$\boldsymbol{N}$	fiber orientation in the reference configuration
$\boldsymbol{n}$	fiber orientation in the deformed configuration
k_1	fiber modulus-like parameter
k_2	fiber dimensionless non-linearity parameter
Π	total energy potential
$\boldsymbol{u}$	displacement field
$\hat{p}$	Lagrange multiplier
$\hat{J}$	kinematic field
$\boldsymbol{\Xi}$	solution of the three-field finite element formulation
$\mathcal{D}$	directional derivative operator

Chapter 1

Introduction

Cardiovascular disorders, especially valve heart diseases, are a principal cause of morbidity and mortality in the world. The requirement for durable, biocompatible heart valve prostheses has generated enormous interests in new materials, innovative designs, and computational simulation techniques. The finite element analysis is a general-purpose tool for simulating and analyzing heart valve biomechanics, enabling researchers to investigate detailed stress distributions and deformation modes under various loading conditions. Convergence of advanced computational methods and novel biomaterials design has significantly empowered the discipline, leading to the development of next-generation heart valve prostheses with improved performance and longevity. In this chapter, the motivation of this research is firstly described. Then, a literature review is provided to highlight several recent progresses in the field of tissue-engineered heart valves as well as the corresponding constitutive modeling and finite element simulations. Lastly, the research objectives of this thesis are summarized.

1.1 Research motivation

According to a study published in 2005, annually around 300,000 valve replacement surgeries are performed worldwide, and this number is predicted to triple in the next three decades due to the increase of the aging population [1]. Traditionally, the most widely adopted artificial heart valves are the mechanical valve and the bioprosthetic valve. The former has the advantage with respect to durability, since it uses materials like pyrolytic carbon and titanium with excellent mechanical strength. However, the mechanical valve has the tendency to cause the formation of a blood clot, and therefore, requires lifetime

anti-coagulation (blood thinning) therapy [2]. The bioprosthetic heart valve is made of bovine or porcine pericardium and has better biocompatibility as well as blood flow dynamics. But it tends to calcify and structurally deteriorate, shortening the service time [3].

Polymeric heart valves are designed to combine the biocompatibility of the bioprosthetic valve and the durability of the mechanical valve. Early researches of polymeric valves mainly use materials like polyurethane. However, due to the absence of bio-stability, mechanical failures tend to happen during cyclic loading conditions [4]. More recent advances in polymeric heart valves introduce high-performance polymers like polyether ether ketone (PEEK), which possess improved blood flow dynamics and the material mechanical properties [5]. Despite the above advances, the adoption of polymeric heart valves is constrained by a number of limitations, such as long-term durability issues and susceptibility to thrombosis and calcification. Current research is focused on improving polymer formulations and processing techniques to develop valves that closely resemble native valve mechanics with improved durability and biocompatibility [6].

With the advancement in tissue engineering, tissue-engineered heart valve (TEHV) provides a promising potential to overcome the drawbacks of existing artificial heart valves [7,8]. With the potential for self-repair, growth, and reduction of long-term complications. TEHVs are designed to integrate into the body's own tissue, gradually adapting to changes in hemodynamic (blood flow) loads over time [9]. However, one of the most significant challenges is to design the scaffold material used in TEHV that closely mimics the mechanical properties of native heart valve tissues. Among various fabrication methods, the electrospinning technology offers an effective approach to fabricate scaffold materials needed in the artificial heart valve. In order to ensure that the fabricated scaffold material mimics the mechanical properties of native valve tissues, solely relying on experimental trial-and-error is labor-intensive, time-consuming, and financially expensive. On the other hand, numerical methods, especially finite element simulations, provide an efficient approach to investigate the mechanical properties of fabricated scaffold materials.

1.2 Literature review

In this section, a brief literature review is provided to highlight several works related to the tissue-engineered heart valves (TEHVs) as well as the corresponding constitutive modeling and finite element simulations. Due to the large amount of research work and publications in these fields, the literature review is by no means exhaustive, but only highlights several recent progresses.

1.2.1 Tissue-engineered heart valves

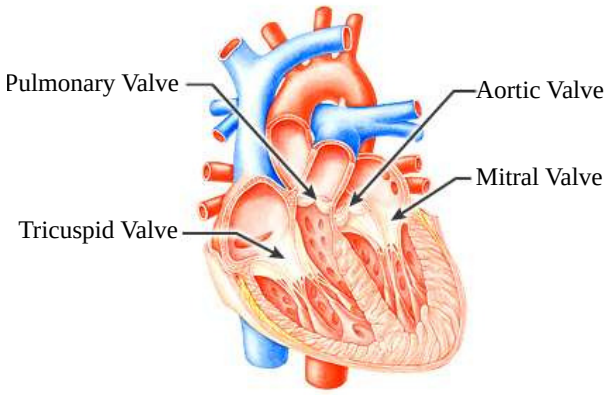

Figure 1.1: Schematics of the four valves of heart, including aortic, pulmonary, tricuspid, and mitral valves (source: http://www.webmd.com/heart-disease/guide/heart-valve-disease).

Valvular heart diseases typically involve the malfunction of one or more of the aortic, pulmonary, tricuspid, and mitral valves, as shown in Fig. 1.1. Intrinsically, the aortic and pulmonary valves show anisotropic mechanical properties due to the unique tri-layered structure, including fibrosa, spongiosa, and ventricularis. The try-layered structure significantly impacts the resistance, elasticity, and resiliency of each valve. The fibrosa layer provides tensile resistance, and the spongiosa layer function as a compressive shock absorber, whereas the ventricularis optimizes leaflet extensibility over the cardiac cycle [10, 11]. Studies of the mechanical properties of natural valves reveal that they can withstand cyclic tensile, shear, and bending stresses during millions of heartbeats annually. Physical properties such as uniaxial and biaxial tensile properties, flexural rigidity, viscoelasticity, and fatigue life have been comprehensively described in native valves but are less well understood in TEHVs. TEHVs must replicate these biomechanical properties in order to withstand physiological loading conditions shortly after implantation as well as long-term usage [12].

Past researches have explored various strategies for enhancing the mechanical function of TEHVs. Early models considered in-vitro tissue remodeling and growth. For instance, several studies emphasized the importance of collagen fiber alignment and extracellular matrix (ECM) deposition for valve durability, see [13,14]. More recent investigations have applied computational modeling techniques to simulate tissue maturation and mechanical behavior. For example, Humphrey and Rajagopal [15] introduced the constrained mixture

models to describe tissue growth, while Gasser et al. [16] used the structural tensor techniques to represent anisotropic tissue responses. Recent advances have been made toward the integration of computational modeling into the TEHV design process to guide the tissue remodeling and improve the valve function. Emmert et al. [17] demonstrated the utility of a computational modeling by creating improved long-term function in a large-animal (sheep) model. This study employed a computationally generated valve geometry to optimize the mechanical performance by reducing non-physiological stress and facilitating the adaptive remodeling. The TEHVs subjected to testing for one year showed sustained function and remodeling comparable to that of natural valves. The adopted computational modeling correctly predicted the tissue remodeling outcomes so that the impact of the mechanical stimuli on cellular behaviors could be well understood. This study allowed the valve geometry and material properties to be optimized for better predictability and safety of TEHVs [17]. The research by Sesa et al. [3] presented a novel mechanical modeling approach to the maturation process of TEHVs, which focused on the bio-hybrid heart valves with the textile scaffold reinforcement. They incorporated an energy-based model to predict the collagen fiber growth during in-vitro maturation, accounting for biological and mechanical growth factors. A finite element method approach was applied using a solid-shell element with the reduced integration, enabling efficient computation of the deformation and stress distribution in the heart valve. Major conclusions indicated that their model can predict the anisotropic tissue behavior with collagen density development influenced by the boundary conditions. This study also highlighted the importance of scaffold design in promoting extracellular matrix (ECM) growth, demonstrating that the textile-reinforced scaffolds provided mechanical supports while allowing progressive tissue remodeling [3].

1.2.2 Constitutive formulation of biological tissues

Constitutive formulation of soft biological tissues is an important research area not only for the design of tissue-engineered heart valves (TEHVs), but also for the general field of biomechanics. Traditional models based on the Green-Lagrange strain tensors and their principal tensor invariants are the foundation for the modeling of tissue mechanics. Tong and Fung [18] pioneered the work of using the Green-Lagrange strain-based models for skin tissue modeling, which were subsequently developed by Fung and Patitucci for arterial mechanics [19]. Chuong and Fung further extended the above work to investigate the stress distribution in arteries [20]. These works are successful in quantifying the nonlinear behaviors of biological tissues. However, they are based on the ideal assumption of perfect

alignment of fibers and hence have limited modeling applicability for biomaterials containing dispersed fiber orientations. Furthermore, they need to satisfy certain mathematical properties such as frame-invariance, incompressibility, and polyconvexity [21].

The significance of fiber dispersion in the mechanics of soft tissues was eventually recognized, which led to the development of more advanced models. Lanir [22] introduced the angular integration approach to account for fiber dispersion in collagenous tissues, which was further enhanced in the work by Gasser et al. with the generalized structure tensor model [16]. These models considered the statistical descriptions of fiber orientations such that tissue microstructure and mechanics could be described more realistically. Motiwale and Sacks [23] further extended these efforts by using meso-structural models for myocardium and electrospun biomaterials and observed the need for mechanical interactions to model tissue behavior with high fidelity in multiple modes of deformation.

On a different front, Jin and Ilinca [24] developed a multiscale modeling approach to simulate the mechanical responses of biological tissues. This method adopted the random walk algorithm to generate the microscopic fiber network structure and then incorporated this network structure into the nonlinear finite element simulations. Moreover, comprehensive mesh convergence analysis and Monte-Carlo simulations were performed to obtain the material mean responses. This approach is further extended to 3D [25] and is successfully used to model the nonlinear behavior of hydrogels [26, 27] and arterial walls [28].

The advent of data-driven approaches has significantly enhanced the research in constitutive modeling. Distance-minimization techniques, introduced by Kirchdoerfer and Ortiz [29], reformulate the boundary value problems in terms of experimental data without the need of using explicit constitutive equations. Alternatively, model-based approaches, i.e., neural networks [30, 31], and spline-based approaches [32], use experimental datasets to construct the adaptive constitutive models. Artificial neural networks, first applied in material modeling by Ghaboussi et al. [30], present an effective approach of modeling sophisticated behavior. But they typically require large data sets for training and computational power. Holzapfel and Ogden [33] included the neural networks within the constitutive modeling frameworks resulting a significant reduction in computational expenses while at the same time maintaining the high fidelity for simulating complex tissue behaviors. Açan et al. [34] developed a novel data-driven constitutive model based on the B-spline approximations integrated with the generalized structure tensor formulation. This approach allows the strain energy function to be decomposed into the volumetric, isotropic, and anisotropic components, where the partial derivatives of the energy function are replaced with B-splines. Their model is flexible, thermodynamically consistent, and provides good fits to several biological tissues .

1.2.3 Finite element modeling of heart valves

Finite element analysis (FEA) has been widely applied to the analysis of heart valve mechanical performance. The early simulations of the heart valve employed generic models based on the hyperelastic material properties [35, 36]. These models were improved using the generalized structure tensor approach in order to more accurately simulate the actual tissue response [16]. Even though these early models provided informative results, they oversimplified complex physiological relationships and required extensive parameter calibration as well as high computational expense, which limited their applications in clinic. In order to eliminate these disadvantages, more realistic geometries began to be incorporated into the finite element (FE) simulations. Inverse finite element analysis techniques allow the estimation of *in vivo* material properties and strains based on the image-derived geometries. For example, Abbasi et al. [37] used the inverse finite element analysis to determine the 3D anisotropic mechanical properties of bovine pericardial leaflets within a surgical bioprosthetic valve. Their technique combines the experimental in-vitro testing with numerical simulations to estimate the material parameters, which are then optimized through the inverse parameter estimation. The study confirms the validity of the application of the 3D anisotropic model for simulating the dynamics of heart valve leaflets under physiological loads, demonstrating the superiority of such a model in more accurately simulating leaflet deformation and stress distributions compared to the simpler isotropic or orthotropic representations.

Other advanced FEA techniques have also aimed at improving the reliability of element formulations used in heart valve analysis. The research by Gilmanov et al. [38] proposed the adoption of a rotation-free shell finite element approach to simulate aortic heart valves. Their approach integrates a nonlinear, anisotropic hyperelastic material model with a shell-based FEA framework to provide a more realistic and efficient formulation of leaflet mechanics. This research uses the rotation-free shell formulation to accommodate complex material responses, thereby enabling high-fidelity simulations of native and bioprosthetic heart valves. Among the major contributions of this work is the comparative study of two constitutive models: the Saint-Venant model, which is an isotropic and simpler formulation, and the May-Newmann–Yin model, which accounts for the anisotropy and fiber reinforcement. Their findings show that the latter more accurately represents the physiological leaflet behavior of heart valves. Their implementation also provided a contact algorithm to model the closure of the valve more realistically while avoiding non-physiological deformations.

On a different front, Balu et al. [39] introduced a novel deep learning framework for the

bioprosthetic valve design and analysis using machine learning to accelerate the simulation-based predictions. Their approach, referred as the Deep Learning-based Finite Element Analysis (DLFEA), replaces the computationally costly FEA simulations with a deep learning surrogate model. The model uses a convolutional autoencoder trained on a large dataset of FEA simulations to predict valve deformation and the coaptation area, which is a key performance measure. The authors also applied a non-uniform rational B-splines (NURBS) informed convolution to accelerate the processing of heart valve geometries without compromising the shape attributes. Experimental results demonstrated that the DLFEA provided good valve deformation predictions with highly accurate coaptation area obtained from the simulation. The framework successfully accounted for the intricate leaflet interactions, such as contact mechanics, without directly including penalty-based contact models. In addition, the methodology generalizes well with various valve geometries and material properties, allowing for fast optimization of bioprosthetic valve designs.

With advancements in medical imaging technologies, patient-specific heart valve modeling has become increasingly realistic. Recently, Laurence et al. [40] developed the FEBio FINESSE, which is an open-source FEA framework used for patient-specific heart valve modeling. It implements a novel approach through the application of a two-stage process under the open-source software FEBio. The FE forward simulations estimate the valve behavior through assumed material properties and approximate the chordae (heart string) representations. Then, a shape constraint algorithm positions the simulated valve shape on 3D echocardiography-based geometries, allowing the accurate estimation of *in vivo* leaflet strains with no need for thorough material characterization. The procedure is validated by synthetic test cases and real patient data, demonstrating its ability to estimate *in vivo* heart valve mechanics with high accuracy.

Mechanical behavior of aortic valve (AV) tissue remains the subject of ongoing research over years due to its complex composition and critical physiological implications. AV tissue is composed predominantly of collagen fibers in a viscid glycosaminoglycan (GAG) matrix, and therefore, is highly anisotropic and viscoelastic. Directional mechanical behavior in the tissue results from the circumferential orientation of collagen fibers and necessitates sophisticated constitutive models that are able to effectively model the similar behaviors. Traditional hyperelastic models are widely employed in simulating AV mechanics. Nevertheless, their inability to incorporate rate-dependent behaviors limits their application, particularly in view of the very high deformation rates *in vivo*. This limitation has led to the development of viscoelastic models that can accommodate time-dependent phenomena such as stress relaxation and creep, which are significant in modeling the full spectrum of AV mechanical responses [41].

For instance, Anssari-Benam et al. [41] developed a transversely isotropic viscoelastic constitutive model specific for AV tissue. The model incorporates the anisotropic response from collagen fiber directions and viscoelastic responses from the tissue's viscous matrix. The model includes both an elastic and a viscous energy function, using the invariants of the right Cauchy-Green deformation tensor and their rates to describe the stress response. Of special interest is that the model can simulate the "shear-thinning" effect observed in AV tissue, for which viscosity decreases with increasing strain rate. Experimental validation was done by conducting uniaxial tensile tests on porcine AV tissue in circumferential and radial directions at a range of strain rates. The model demonstrated excellent agreement with the experimental results and accurately reproduced the stress-deformation response in physiological conditions. Its ability to handle both anisotropic and rate-dependent behavior makes it a significant step forward comparing with standard hyperelastic theories.

The mitral valve (MV) also plays a central role in the proper functioning of the heart. The need for accurate computational models of the MV has spurred research focusing on its complex multi-layered structure and mechanical properties. One of the significant contributions is the development of a meso-scale layer-specific structural constitutive model of the MV leaflets from Zhang et al. [42]. Traditional models of the MV do not account for the complexity of its structure in terms of how each of the four layers functions mechanically: the ventricularis, fibrosa, spongiosa, and atrialis. The proposed meso-scale layer-specific model improves this limitation with the added layer-specific structure information in terms of collagen and elastin fiber networks that govern the mechanical responses of the leaflets. Measuring the orientation and distribution of fibers in each of the layers was achieved through the use of second harmonic generation (SHG) microscopy and histology. A key improvement of the above model is its inclusion of the orientation-dependent recruitment of collagen fibers, which deviates from previous models assuming orientation-invariant recruitment. This enhancement enables the model to more accurately describe the anisotropic, nonlinear mechanical properties of the MV leaflets, particularly under the surgically induced extra-physiological loading regimes present after surgery. The model was further validated by large amounts of biaxial mechanical testing data, in addition to small-angle X-ray scattering studies, which demonstrated its predictive accuracy at both the tissue and fibril levels. The meso-scale layer-specific model can correctly estimate the mean effective collagen fiber modulus and exhibited good agreement with experimental results, which again confirmed its validity for simulating MV mechanics [42].

1.3 Research objectives

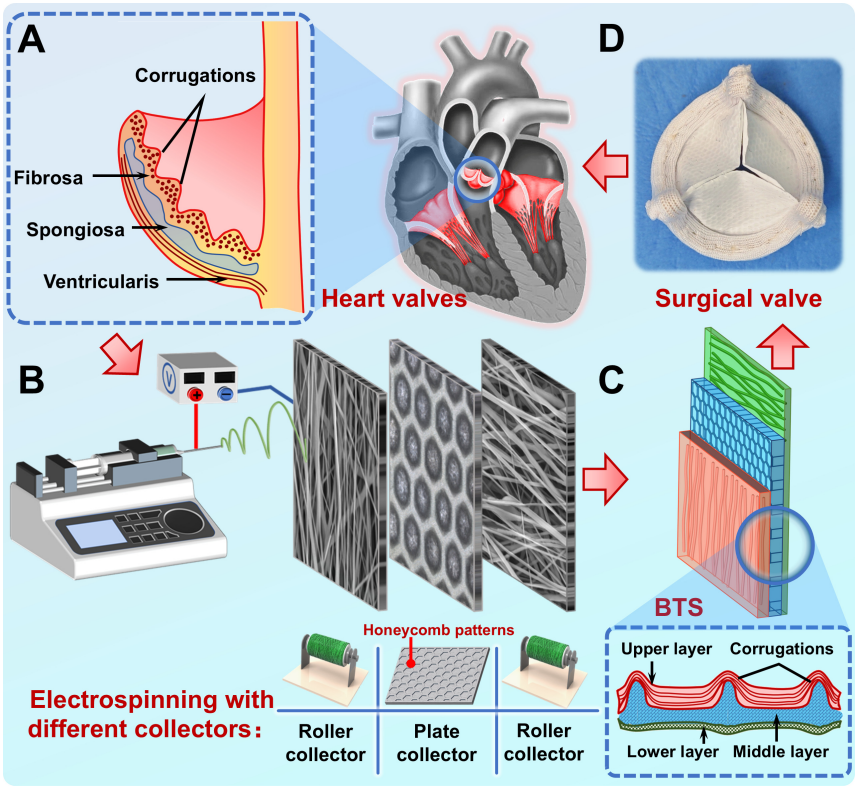

Figure 1.2: Schematic of the fabrication process of the biomimetic tri-layer scaffold for surgical heart valve (courtesy of Dr. Xing Zhang, Chinese Academy of Sciences): (a) heart valve with the tri-layer structure, including fibrosa, spongiosa, and ventricularis; (b) reparation of the upper, middle, and lower layers with different fiber morphology by electrostatic spinning with different collectors; (c) the assembled biomimetic tri-layer scaffold; and (d) the surgical heart valve using the fabricated tri-layer scaffold.

Among various fabrication methods, the electrospinning technology offers an effective approach to fabricate scaffold materials needed in the artificial heart valve. Figure 1.2 illustrates the fabrication process of the biomimetic tri-layer scaffold for surgical heart valve, developed by the research team of Dr. Xing Zhang from the Chinese Academy of Sciences. They discovered that the electrostatic spinning technique could be used to fabricate various layers that mimic the fiber alignments inside the layers of native valve tissues, including the fibrosa, spongiosa, and ventricularis layer. In this tri-layer structure, the top layer and the bottom layer contain two sets of orthogonal fibers, while the middle layer contains a series of honeycomb patterns. In this process, the crucial step is to design the tri-layer scaffold that closely mimic the mechanical properties of native valve

tissues. Particularly, the geometric arrangement of the honeycomb patterns contained in the middle layer, as shown in Fig. 1.3, can significantly impact the nonlinear behavior of the tri-layer scaffold and its anisotropy.

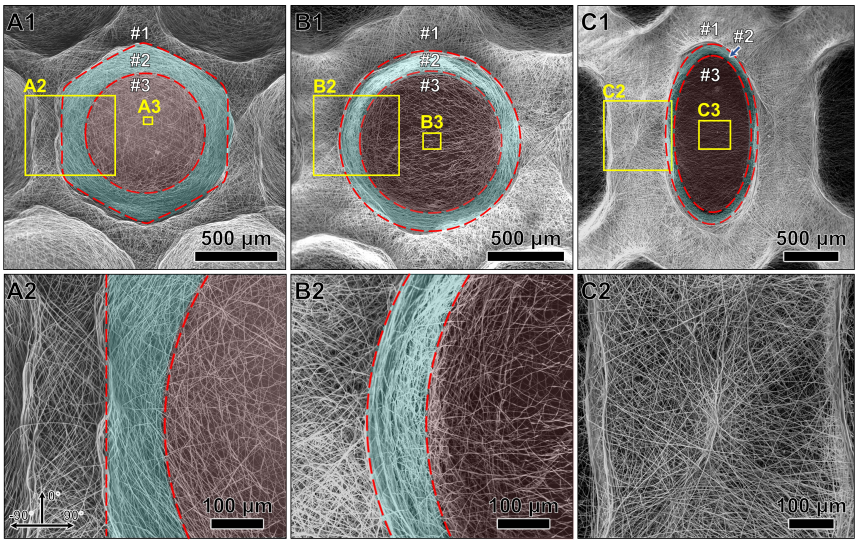

Figure 1.3: The honeycomb pattern contained in the middle layer of the tri-layer scaffold (courtesy of Dr. Xing Zhang, Chinese Academy of Sciences), the geometry of which can significantly impact the material nonlinear behavior and anisotropy.

In order to ensure that the fabricated tri-layer scaffold material mimics the mechanical properties of native valve tissues, solely relying on experimental trial-and-error is labor-intensive, time-consuming, and financially expensive. On the other hand, numerical methods, especially finite element simulations, provide an efficient approach to investigate the mechanical properties of fabricated scaffold and guide the sample design. *The focus of this thesis is to develop a computational framework based on the finite element method to model the mechanical responses of the bioinspired tri-layer scaffold used for heart valve constructs*. Specifically, the following tasks are accomplished:

- A hyperelastic constitutive model is adopted for the tri-layer scaffold. The total strain energy function involves the classical impressible neo-Hookean model and a polynomial-form anisotropic model [25]. This material model uses the structural tensors to describe the material anisotropy and can accurately describe the material nonlinear behavior.

- A three-field mixed finite element procedure is adopted to enforce the material incompressibility and avoid the volumetric locking, which is typically encountered in the numerical modeling of biomaterials.

- The finite element model is created for the tri-layer scaffold material sample. Particularly, the geometry and composition of the honeycomb patterns contained in the middle layer are properly considered, which significantly impact the material anisotropy.
- The numerical results are compared with the experimental observations to demonstrate the effectiveness and accuracy of the developed computational framework.

The remaining part of the thesis is organized as follows. In Chapter 2, the major results of the nonlinear solid mechanics are presented, which provide the theoretical foundation of the general hyperelastic constitutive modeling. Particularly, various constitutive formulation techniques for incompressible materials are discussed. In Chapter 3, the constitutive model for the biomimetic tri-layer scaffold is developed, and the three-field mixed finite element formulation is presented to enforce the material incompressibility. In Chapter 4, the numerical results obtained from the proposed computational framework are presented, which are then compared with the experimental observations of the mechanical test of the tri-layer scaffold. Chapter 5 summarizes the conclusions of this research and discusses several avenues to further improve the developed numerical technique. All the source codes developed in this thesis are hosted on GitHub[1] to support the movement of open science.

[1] https://github.com/taojinllnl/

Chapter 2

Preliminaries

Biomaterials typically go through finite (large) deformation under physiological loading conditions. Therefore, nonlinear solid mechanics should be used for the theoretical analysis and numerical modeling of biomaterials such as heart valve tissues. In this chapter, the major conclusions derived from the theory of nonlinear solid mechanics are presented, which form the foundation of the subsequent finite element modeling. Moreover, biomaterials are typically incompressible. Several techniques, such as the Lagrange multiplier method and the penalty method, are briefly discussed to consider the material incompressibility constraint. This thesis adopts the following conventions. Lowercase regular letters (e.g., α, β) represent scalars. Uppercase bold letters (e.g., $\mathbf{C}$, $\mathbf{S}$) denote vectors and tensors in the reference (undeformed) configuration. Lowercase bold letters (e.g., $\mathbf{b}$, $\boldsymbol{\sigma}$) represent vectors and tensors in the current (deformed) configuration.

2.1 Brief review of nonlinear solid mechanics

The theory of nonlinear solid mechanics forms the foundation of the constitutive modeling and the finite element simulation in the finite (large) deformation regime. Therefore, for the sake of the completeness of the thesis, several important conclusions about the kinematics, the stress and force equilibrium, as well as the framework of hyperelasticity are briefly reviewed in this section. These conclusions are mainly selected from the classical text book by Bonet and Wood [43].

2.1.1 Kinematics

A continuum in the reference configuration, denoted as $\Omega_0 \subset \mathbb{R}^3$, undergoes a deformation $\boldsymbol{\phi}$ under static loading conditions. Each particle $\boldsymbol{X}$ in the reference configuration Ω_0 is mapped to a corresponding point $\boldsymbol{x}$ in the deformed configuration $\Omega \subset \mathbb{R}^3$ according to the following relationship:

$$\boldsymbol{x} = \boldsymbol{\phi}(\boldsymbol{X})$$

The deformation gradient is defined as:

$$\mathbf{F} = \frac{\partial \phi}{\partial \boldsymbol{X}} = \frac{\partial \boldsymbol{x}}{\partial \boldsymbol{X}}. \tag{2.1}$$

The above definition can also be expressed in the index form as:

$$\mathbf{F} = F_{iJ}\, \boldsymbol{e}_i \otimes \boldsymbol{E}_J, \quad F_{iJ} = \frac{\partial x_i}{\partial X_J}, \quad i, J = 1, 2, 3, \tag{2.2}$$

Where $\boldsymbol{E}_i$ denotes the Cartesian basis vectors in the reference (undeformed) configuration, and $\boldsymbol{e}_i$ denotes the basis vectors in the deformed configuration. Consider $d\boldsymbol{L}$, $d\boldsymbol{A}$, and dV as the line element, area element, and volume element in the reference configuration, respectively. Their counterparts in the deformed configuration $d\boldsymbol{l}$, $d\boldsymbol{a}$, and dv are obtained via the following relationships:

$$d\boldsymbol{l} = \mathbf{F}\, d\mathbf{L}, \quad d\boldsymbol{a} = (\operatorname{adj} \mathbf{F})^{\mathrm{T}}\, d\mathbf{A}, \quad dv = J\, dV$$

where $J = \det \mathbf{F}$ and $\operatorname{adj}(\mathbf{F}) = J\mathbf{F}^{-1}$ denote the determinant and the adjugate of the deformation gradient, respectively.

Consider the element vectors $d\boldsymbol{X}_1$ and $d\boldsymbol{X}_2$ in the reference configuration, which deform to $d\boldsymbol{x}_1$ and $d\boldsymbol{x}_2$ in the deformed configuration. The inner product $d\boldsymbol{x}_1 \cdot d\boldsymbol{x}_2$ can be expressed in terms of the material vectors $d\boldsymbol{X}_1$ and $d\boldsymbol{X}_2$ as:

$$d\boldsymbol{x}_1 \cdot d\boldsymbol{x}_2 = d\boldsymbol{X}_1 \cdot \mathbf{C}\, d\boldsymbol{X}_2. \tag{2.3}$$

In the above equation, C is the right Cauchy-Green deformation tensor, which is expressed in terms of the deformation gradient $\mathbf{F}$ as:

$$\mathbf{C} = \mathbf{F}^{\mathrm{T}}\mathbf{F}. \tag{2.4}$$

Similarly, the material inner product $d\boldsymbol{X}_1 \cdot d\boldsymbol{X}_2$ can be obtained in terms of the spatial vectors $d\boldsymbol{x}_1$ and $d\boldsymbol{x}_2$ as:

$$d\boldsymbol{X}_1 \cdot d\boldsymbol{X}_2 = d\boldsymbol{x}_1 \cdot \mathbf{b}^{-1} d\boldsymbol{x}_2, \tag{2.5}$$

where $\mathbf{b}$ is the left Cauchy-Green deformation tensor defined as:

$$\mathbf{b} = \mathbf{F}\mathbf{F}^{\mathrm{T}}. \tag{2.6}$$

The change in the scalar product can be expressed in terms of the material vectors $d\boldsymbol{X}_1$ and $d\boldsymbol{X}_2$ and the the spatial vectors $d\boldsymbol{x}_1$ and $d\boldsymbol{x}_2$ as:

$$\frac{1}{2}\big(d\boldsymbol{x}_1 \cdot d\boldsymbol{x}_2 - d\boldsymbol{X}_1 \cdot d\boldsymbol{X}_2\big) = d\boldsymbol{X}_1 \cdot \mathbf{E}\, d\boldsymbol{X}_2 = d\boldsymbol{x}_1 \cdot \mathbf{e}\, d\boldsymbol{x}_2, \tag{2.7}$$

where the Lagrangian-Green strain tensor $\mathbf{E}$ and the Eulerian (Almansi) strain tensor $\mathbf{e}$ are expressed as:

$$\mathbf{E} = \frac{1}{2}(\mathbf{C} - \mathbf{I}) \tag{2.8}$$

and

$$\mathbf{e} = \frac{1}{2}\big(\mathbf{I} - \mathbf{b}^{-1}\big). \tag{2.9}$$

The deformation gradient $\mathbf{F}$ can be further split into the stretch and rotation components as:

$$\mathbf{F} = \mathbf{R}\mathbf{U}, \tag{2.10}$$

where $\mathbf{R}$ is the rotation tensor, and $\mathbf{U}$ is the stretch tensor. As the rotation tensor is orthogonal, the right Cauchy-Green tensor $\mathbf{C}$ can be expressed as

$$\mathbf{C} = \mathbf{F}^{\mathrm{T}}\mathbf{F} = \mathbf{U}^{\mathrm{T}}\mathbf{R}^{\mathrm{T}}\mathbf{R}\mathbf{U} = \mathbf{U}^2. \tag{2.11}$$

The above equation reveals that the right Cauchy-Green tensor $\mathbf{C}$ is rotation-free and only contains the stretch information. Similarly, the deformation gradient $\mathbf{F}$ is decomposed in the spatial configuration by the spatial stretch tensor $\mathbf{V}$ and the rotation tensor $\mathbf{R}$ as:

$$\mathbf{F} = \mathbf{V}\mathbf{R}. \tag{2.12}$$

Then, the left Cauchy-Green tensor can be expressed as:

$$\mathbf{b} = \mathbf{F}\mathbf{F}^{\mathrm{T}} = (\mathbf{V}\mathbf{R})(\mathbf{R}^{\mathrm{T}}\mathbf{V}) = \mathbf{V}^2. \tag{2.13}$$

The above equation indicates that $\mathbf{b}$ is also rotation-free and only contains the stretch information.

For incompressible and nearly incompressible materials, it is typical to separate the volumetric component and the distortional component from the deformation gradient, that is

$$\mathbf{F} = J^{1/3}\bar{\mathbf{F}}. \tag{2.14}$$

It can be verified that

$$\det \bar{\mathbf{F}} = 1. \tag{2.15}$$

Therefore,

$$\bar{\mathbf{F}} = J^{-1/3}\mathbf{F} \tag{2.16}$$

only represents the shape change and is free from the volumetric change. As a result, the distortional part of the right Cauchy-Green tensor $\mathbf{C}$ and the left Cauchy-Green tensor are defined as:

$$\bar{\mathbf{C}} = \bar{\mathbf{F}}^{\mathrm{T}}\bar{\mathbf{F}} = J^{-2/3}\mathbf{C} \tag{2.17}$$

and

$$\bar{\mathbf{b}} = \bar{\mathbf{F}}\bar{\mathbf{F}}^{\mathrm{T}} = J^{-2/3}\mathbf{b}. \tag{2.18}$$

2.1.2 Stress and force equilibrium

In the framework of nonlinear solid mechanics, there are various stress measures, such as the Cauchy stress $\boldsymbol{\sigma}$, the 1st Piola-Kirchhoff (1st P-K) stress $\mathbf{P}$, the 2nd Piola-Kirchhoff (2nd P-K) stress $\mathbf{S}$, and the Kirchhoff stress tensor $\boldsymbol{\tau}$, depending on either the reference (undeformed) configuration or current (deformed) configuration is under discussion. These stress measures are connected through the deformation gradient $\mathbf{F}$. Here are some commonly used relationships among the above stress measures:

$$\boldsymbol{\sigma} = J^{-1}\mathbf{F}\mathbf{S}\mathbf{F}^{\mathrm{T}} = J^{-1}\mathbf{P}\mathbf{F}^{\mathrm{T}}, \quad \mathbf{P} = \mathbf{F}\mathbf{S}, \quad \boldsymbol{\tau} = J\boldsymbol{\sigma}. \tag{2.19}$$

For the above relationships, it can be seen that the Cauchy stress $\boldsymbol{\sigma}$ and the Kirchhoff stress $\boldsymbol{\tau}$ are measures with respect to the deformed configuration Ω. The 2nd P-K stress $\mathbf{S}$ is a stress measure with respect to the reference configuration Ω_0. The 1st P-K stress $\mathbf{P}$ is a particular case, which functions as a so-called two-point tensor between the reference configuration and the deformed configuration.

Depending on which stress measure is adopted, the internal virtual work δW_{int} can be expressed in different but equivalent forms:

$$\delta W_{\mathrm{int}} = \int_{\Omega} \boldsymbol{\sigma} : \delta\mathbf{e}\, dv = \int_{\Omega_0} \mathbf{P} : \delta\mathbf{F}\, dV = \int_{\Omega_0} \mathbf{S} : \delta\mathbf{E}\, dV. \tag{2.20}$$

In the above equation, $\delta\mathbf{e}$ is the virtual Almansi strain tensor, $\delta\mathbf{E}$ is the virtual Lagrange-Green strain tensor, while $\delta\mathbf{F}$ is the virtual deformation gradient. The double contraction operation is defined as:

$$\mathbf{A} : \mathbf{B} = A_{ij}B_{ij}, \tag{2.21}$$

in which the Einstein summation is adopted. Therefore, $\boldsymbol{\sigma}$ and $\mathbf{e}$, $\mathbf{P}$ and $\mathbf{F}$, as well as $\mathbf{S}$ and $\mathbf{E}$ form three work-conjugate pairs. Notice that the first integration is with respect to the deformed configuration Ω, while the other two are with respect to the reference configuration Ω_0.

In solid mechanics, the governing equations of the deformation body are the balances of the linear momentum and the angular momentum. The balance of the angular momentum is expressed by the symmetry of the Cauchy stress tensor, that is, $\boldsymbol{\sigma} = \boldsymbol{\sigma}^{\mathrm{T}}$. The balance of the linear momentum, which acts as the governing partial differential equation (PDE) for the finite element simulation of the deformed body, can be written either with respect to the deformed (spatial) configuration or the undeformed (reference) configuration. Assuming the problem is static, in the deformed configuration,

$$\mathrm{div}\boldsymbol{\sigma} + \boldsymbol{f} = \mathbf{0} \quad \text{in} \quad \Omega. \tag{2.22}$$

In the reference configuration, the same balance of linear momentum equation can be rewritten as

$$\mathrm{Div}\mathbf{P} + \boldsymbol{f}_0 = \mathbf{0} \quad \text{in} \quad \Omega_0. \tag{2.23}$$

In the above two equations, $\boldsymbol{f}$ and $\boldsymbol{f}_0$ represent the body force in the deformed configuration and the reference configuration, respectively. One of the above governing equations, combined with the appropriate boundary conditions and the material constitutive model, form the strong form of the deformed body under external loading conditions.

2.1.3 Hyperelasticity

As mentioned before, a material constitutive model that establishes the stress-strain relationship is needed for nonlinear finite element simulation of solid mechanics problems. A material is classified as hyperelastic if the work done by the stresses during a deformation process is path-independent. That is, the work only depends on the initial configuration and the final configuration. As shown in Eq. (2.20), the 1st P-K stress $\mathbf{P}$ is work conjugate with respect to the deformation gradient $\mathbf{F}$, therefor, the 1st P-K stress can be derived from the elastic strain energy Ψ as

$$\mathbf{P}(\mathbf{F}(\boldsymbol{X}), \boldsymbol{X}) = \frac{\partial \Psi(\mathbf{F}(\boldsymbol{X}), \boldsymbol{X})}{\partial \mathbf{F}}, \tag{2.24}$$

where $\boldsymbol{X}$ represents the material location. Note that as shown in Eq. (2.10), the deformation gradient $\mathbf{F}$ contains rotation information. However, the strain energy function Ψ should remain invariant under a rigid body rotation, which is called frame-indifference.

This requirement implies that Ψ should depend on $\mathbf{F}$ only through the stretch component $\mathbf{U}$ and is independent from the rotational component $\mathbf{R}$. As a result, Ψ is expressed as a function of $\mathbf{C}$ as:

$$\Psi(\mathbf{F}, \boldsymbol{X}) = \Psi(\mathbf{C}, \boldsymbol{X}), \tag{2.25}$$

where $\mathbf{C} = \mathbf{U}^2 = \mathbf{F}^{\mathrm{T}}\mathbf{F}$. The 2nd Piola-Kirchhoff (P-K) stress $\mathbf{S}$ is expressed as:

$$\mathbf{S}(\mathbf{C}, \mathbf{X}) = 2\frac{\partial \Psi}{\partial \mathbf{C}} = \frac{\partial \Psi}{\partial \mathbf{E}}, \tag{2.26}$$

Where $\mathbf{E}$ is the Green-Lagrange strain tensor defined in Eq. (2.8).

By linearizing with respect to an increment $\boldsymbol{u}$, the directional derivative of the 2nd P-K stress $\mathbf{S}$ with respect to the Green-Lagrange strain tensor $\mathbf{E}$ is expressed as:

$$D\mathbf{S}[\boldsymbol{u}] = \mathbb{C} : D\mathbf{E}[\boldsymbol{u}] \tag{2.27}$$

where the material elasticity tensor $\mathbb{C}$ is a symmetric fourth-order tensor expressed as:

$$\mathbb{C} = \frac{\partial \mathbf{S}}{\partial \mathbf{E}} = 4\frac{\partial^2 \Psi}{\partial \mathbf{C} \partial \mathbf{C}} = 4\frac{\partial^2 \Psi}{\partial C_{IJ} \partial C_{KL}} \boldsymbol{E}_I \otimes \boldsymbol{E}_J \otimes \boldsymbol{E}_K \otimes \boldsymbol{E}_L. \tag{2.28}$$

The above stress-strain relationship can also be expressed in the deformed configuration. The Cauchy stress tensor $\boldsymbol{\sigma}$ is defined as

$$\boldsymbol{\sigma}(\mathbf{b}, \mathbf{x}) = 2J^{-1}\frac{\partial \Psi}{\partial \mathbf{b}}\mathbf{b} = 2J^{-1}\mathbf{b}\frac{\partial \Psi}{\partial \mathbf{b}}. \tag{2.29}$$

Similar, the spatial elasticity tensor $\mathbf{c}$ is defined as

$$\begin{aligned} \mathbf{c} &= 4J^{-1}\boldsymbol{b}\frac{\partial^2 \Psi}{\partial \boldsymbol{b}^2}\boldsymbol{b} \\ &= 4J^{-1}b_{im}\frac{\partial^2 \Psi}{\partial b_{mj} \partial b_{kn}} b_{nl}\ \boldsymbol{e}_i \otimes \boldsymbol{e}_j \otimes \boldsymbol{e}_k \otimes \boldsymbol{e}_l. \end{aligned} \tag{2.30}$$

The relationship between the 2nd P-K stress tensor $\mathbf{S}$ and the Cauchy stress tensor $\boldsymbol{\sigma}$ is expressed in Eq. (2.19). The relationship between the spatial elasticity tensor $\mathbf{c}$ and the material elasticity tensor is is expressed as

$$\mathbf{c} = J^{-1}F_{iI}F_{jJ}F_{kK}F_{lL}C_{IJKL}\boldsymbol{e}_i \otimes \boldsymbol{e}_j \otimes \boldsymbol{e}_k \otimes \boldsymbol{e}_l. \tag{2.31}$$

For isotropic materials, since the constitutive behavior is identical in all material directions, the strain energy function Ψ can be expressed solely by the principal invariants of $\mathbf{C}$ or $\mathbf{b}$, that is:

$$\Psi(\mathbf{C}, \boldsymbol{X}) = \Psi(I_1, I_2, I_3, \boldsymbol{X}) \tag{2.32}$$

Where the three principal tensor invariants are defined as:

$$I_1 = \mathrm{tr}(\mathbf{C}) = \mathrm{tr}(\mathbf{b}), \tag{2.33}$$

$$I_2 = \frac{1}{2}[\mathrm{tr}^2(\mathbf{C}) - \mathrm{tr}(\mathbf{C}^2)] = \frac{1}{2}[\mathrm{tr}^2(\mathbf{b}) - \mathrm{tr}(\mathbf{b}^2)], \tag{2.34}$$

$$I_3 = \mathrm{det}\mathbf{C} = \mathrm{det}\mathbf{b} = (\mathrm{det}\mathbf{F})^2 = J^2. \tag{2.35}$$

As shown previously, the derivation of the 2nd P-K stress or the Cauchy stress involves partial derivatives. The corresponding derivatives of the principal tensor invariants can be expressed as:

$$\frac{\partial I_1}{\partial \mathbf{C}} = \mathbf{I}, \quad \frac{\partial I_1}{\partial \mathbf{b}} = \mathbf{I}, \tag{2.36}$$

$$\frac{\partial I_2}{\partial \mathbf{C}} = I_1\mathbf{I} - \mathbf{C}, \quad \frac{\partial I_2}{\partial \mathbf{b}} = I_1\mathbf{I} - \mathbf{b}, \tag{2.37}$$

$$\frac{\partial I_3}{\partial \mathbf{C}} = I_3\mathbf{C}^{-1}, \quad \frac{\partial I_3}{\partial \mathbf{b}} = I_3\mathbf{b}^{-1}, \tag{2.38}$$

where $\mathbf{I}$ represents the second-order identity tensor. Recall that $J = \mathrm{det}\mathbf{F}$, therefore,

$$\frac{\partial J}{\partial \mathbf{C}} = \frac{\partial J}{\partial J^2}\frac{\partial J^2}{\partial \mathbf{C}} = \frac{1}{2}J^{-1}\frac{\partial I_3}{\partial \mathbf{C}} = \frac{J}{2}\mathbf{C}^{-1}. \tag{2.39}$$

Similarly,

$$\frac{\partial J}{\partial \mathbf{b}} = \frac{\partial J}{\partial J^2}\frac{\partial J^2}{\partial \mathbf{b}} = \frac{1}{2}J^{-1}\frac{\partial I_3}{\partial \mathbf{b}} = \frac{J}{2}\mathbf{b}^{-1}. \tag{2.40}$$

2.2 Material incompressibility

Biomaterials are typically incompressible, that is, the deformation gradient $\mathbf{F}$ should satisfy the following incompressibility constraint:

$$\mathrm{det}\mathbf{F} = J = 1.$$

At the constitutive model level, there are two commonly adopted approaches to model the material incompressibility, the penalty method and the Lagrange multiplier method.

2.2.1 Penalty method

The basic idea of the penalty method to enforce the material incompressibility constraint is to make the material slightly compressible (or nearly incompressible), that is,

$$\mathrm{det}\mathbf{F} = J \approx 1.$$

The total strain energy function is usually decomposed into two terms:

$$\Psi = U(J) + \Psi_{\text{dev}}(\bar{\mathbf{C}}), \tag{2.41}$$

where $U(J)$ is the volumetric term representing the strain energy caused by the material volumetric change, and $\Psi_{\text{dev}}(\bar{\mathbf{C}})$ is the distortional term representing the strain energy caused by the material shape change. The volumetric term $U(J)$ contains the bulk modulus parameter K, which serves as the penalty parameter to penalize any volumetric deformation. For instance, one example of the typically adopted $U(J)$ form is

$$U(J) = \frac{K}{2}(J-1)^2.$$

Then, the 2nd P-K stress can be derived as:

$$\mathbf{S} = 2\frac{\partial U(J)}{\partial J}\frac{\partial J}{\partial \mathbf{C}} + 2\frac{\partial \Psi_{\text{dev}}(\bar{\mathbf{C}})}{\partial \mathbf{C}}, \tag{2.42}$$

In this approach, the penalty parameter (bulk modulus) K should be a large number to effectively enforce the material incompressibility constraint. However, when K is too large, the condition number of the finite element stiffness matrix will significantly increase, causing convergence difficulties during the nonlinear iterations. Therefore, it is important to balance between the above two considerations and choose a proper value of the penalty parameter K.

2.2.2 Lagrange multiplier method

Using the Lagrange multiplier method to enforce the material incompressibility constraint, the material is treated as strictly incompressible, that is,

$$\det\mathbf{F} = J = 1.$$

Based on the above constraint,

$$\mathbf{C} = \bar{\mathbf{C}}.$$

Therefore, the hyperelastic strain energy becomes

$$\Psi = \Psi(\mathbf{C}) = \Psi(\bar{\mathbf{C}}). \tag{2.43}$$

The corresponding 2nd P-K stress is expressed as:

$$\mathbf{S} = pJ\mathbf{C}^{-1} + 2\frac{\partial \Psi(\bar{\mathbf{C}})}{\partial \mathbf{C}}, \tag{2.44}$$

where the pressure term p acts as the Lagrange multiplier to enforce the material incompressibility. Even though this approach does not require to select the penalty parameter as needed in the penalty method, extra fields such as the Lagrange multiplier p and the volumetric change J are introduced into the constitutive formulation, which typically requires a mixed finite element formulation.

2.3 Summary

In this section, several important results related to the nonlinear solid mechanics are presented, including the kinematics, various stress measures, material hyperelasticity, and two constitutive modeling techniques to enforce the material incompressibility constraint. These results form the foundation for the nonlinear finite element modeling of the biomimetic tri-layer scaffold material.

Chapter 3

Constitutive modeling and mixed formulation

In this chapter, the computational framework to model the mechanical behavior of the biomimetic tri-layer scaffold material is presented. This computational framework includes two major components, the hyperelastic constitutive model and the three-field mixed finite element formulation. The former is designed to reflect the impact of the material microscopic structure such as fiber orientation on the material stress-strain relationship, while the latter is necessary to enforce the material incompressibility without causing the volumetric locking. The computational framework is programmed in deal.II [44], which is an open-source C++ finite element library. All the source codes developed in this thesis are hosted on GitHub[1] to support the movement of open science.

3.1 Constitutive modeling

Finite element modeling is an effective approach to investigate the structure-function relationship of various biological tissues and bio-inspired materials [26, 28]. Most biomaterials are incompressible and typically go through large (finite) deformation under external loading conditions. Therefore, the finite element techniques capable of considering finite deformation and material incompressibility are needed for the modeling of the biomimetic tri-layer scaffolds. In this work, the following hyperelastic strain energy function is adopted as:

$$\Psi = U(J) + \Psi_{\text{iso}}(\bar{\mathbf{C}}) + \Psi_{\text{aniso}}(\mathbf{C}), \tag{3.1}$$

[1] https://github.com/taojinllnl/

where U represents the strain energy associated with the material volume change, Ψ_{iso} represents the isotropic part of the total strain energy caused by the shape change, and Ψ_{aniso} represents the anisotropic part of the total strain energy contributed by the fiber components. Notice that the anisotropic part of the strain energy should depend on the full right Cauchy-Green tensor $\mathbf{C}$, instead of its distortional part $\bar{\mathbf{C}}$. For a detailed discussion, see [21, 45–47].

In this work, the incompressible neo-Hookean model is adopted, that is,

$$U(J) = \frac{1}{2}K(J-1)^2 \tag{3.2}$$

and

$$\Psi_{\text{iso}}(\bar{\mathbf{C}}) = \frac{1}{2}G(\bar{I}_1 - 3), \tag{3.3}$$

where K is the material bulk modulus, G is the material shear modulus, $J = \det\mathbf{F}$ is the determinant of the deformation gradient $\mathbf{F}$ reflecting the material volume change, $\bar{\mathbf{C}} = J^{-2/3}\mathbf{C}$ is the distortional part of the right Cauchy-Green tensor, and $\bar{I}_1 = \text{tr}\bar{\mathbf{C}}$ is its first principal invariant. In the above equation, the volumetric strain energy $U(J)$ serves as a penalty term, and the bulk modulus K can be considered as a penalty parameter. Then, the 2nd P-K (Piola-Kirchhoff) stress tensor for the volumetric term can be expressed as:

$$\mathbf{S}_{\text{vol}} = 2\frac{\partial U(J)}{\partial \mathbf{C}} = 2\frac{\partial U(J)}{\partial J}\frac{\partial J}{\partial \mathbf{C}} = pJ\mathbf{C}^{-1}, \tag{3.4}$$

where the pressure term

$$p = \frac{\partial U(J)}{\partial J} = K(J-1).$$

The 2nd P-K stress tensor for the isotropic term is

$$\mathbf{S}_{\text{iso}} = 2\frac{\partial \Psi_{\text{iso}}(\bar{\mathbf{C}})}{\partial \mathbf{C}} = GJ^{-\frac{2}{3}}(\mathbf{I} - \frac{1}{3}I_1\mathbf{C}^{-1}). \tag{3.5}$$

In the deformed configuration, the corresponding Cauchy stress tensors are

$$\boldsymbol{\sigma}_{\text{vol}} = J^{-1}\mathbf{F}\mathbf{S}_{\text{vol}}\mathbf{F}^{\text{T}} = p\mathbf{I} \tag{3.6}$$

and

$$\boldsymbol{\sigma}_{\text{iso}} = J^{-1}\mathbf{F}\mathbf{S}_{\text{iso}}\mathbf{F}^{\text{T}} = GJ^{-1}(\bar{\mathbf{b}} - \frac{1}{3}\bar{I}_1\mathbf{I}). \tag{3.7}$$

The corresponding material elasticity tensors in the reference configuration are

$$\mathbb{C}_{\text{vol}} = 4\frac{\partial^2 U(J)}{\partial \mathbf{C}^2} = 2pJ\frac{\partial \mathbf{C}^{-1}}{\partial \mathbf{C}} + J(p + KJ)\mathbf{C}^{-1} \otimes \mathbf{C}^{-1} \tag{3.8}$$

and

$$\begin{aligned}\mathbb{C}_{\text{iso}} &= 4\frac{\partial^2 \Psi_{\text{iso}}(\bar{\mathbf{C}})}{\partial \mathbf{C}^2} \\ &= -\frac{2}{3}GJ^{-2/3}(\mathbf{I}\otimes\mathbf{C}^{-1}+\mathbf{C}^{-1}\otimes\mathbf{I}) + \frac{2}{3}GJ^{-2/3}I_1\left(\frac{1}{3}\mathbf{C}^{-1}\otimes\mathbf{C}^{-1} - \frac{\partial \mathbf{C}^{-1}}{\partial \mathbf{C}}\right).\end{aligned} \tag{3.9}$$

The corresponding spatial elasticity tensors are

$$\mathbf{c}_{\text{vol}} = 4J^{-1}\boldsymbol{b}\frac{\partial^2 U(J)}{\partial \boldsymbol{b}^2}\boldsymbol{b} = -p(\mathbb{I}+\bar{\mathbb{I}}) + (p+KJ)\mathbf{I}\otimes\mathbf{I} \tag{3.10}$$

and

$$\begin{aligned}\mathbf{c}_{\text{iso}} &= 4J^{-1}\boldsymbol{b}\frac{\partial^2 \Psi_{\text{iso}}}{\partial \boldsymbol{b}^2}\boldsymbol{b} \\ &= -\frac{2}{3}GJ^{-5/3}(\mathbf{b}\otimes\mathbf{I}+\mathbf{I}\otimes\mathbf{b}) + \frac{2}{3}GJ^{-5/3}I_1\left(\frac{1}{3}\mathbf{I}\otimes\mathbf{I} + \frac{\mathbb{I}+\bar{\mathbb{I}}}{2}\right).\end{aligned} \tag{3.11}$$

The above equations involve several fourth-order tensors that are defined as below:

$$\frac{\partial \mathbf{C}^{-1}}{\partial \mathbf{C}} = -\frac{1}{2}(C^{-1}_{IK}C^{-1}_{JL} + C^{-1}_{IL}C^{-1}_{JK})\boldsymbol{E}_I\otimes\boldsymbol{E}_J\otimes\boldsymbol{E}_K\otimes\boldsymbol{E}_L, \tag{3.12}$$

$$\mathbb{I} = \delta_{ik}\delta_{jl}\boldsymbol{e}_i\otimes\boldsymbol{e}_j\otimes\boldsymbol{e}_k\otimes\boldsymbol{e}_l = \boldsymbol{e}_i\otimes\boldsymbol{e}_j\otimes\boldsymbol{e}_i\otimes\boldsymbol{e}_j, \tag{3.13}$$

$$\bar{\mathbb{I}} = \delta_{il}\delta_{jk}\boldsymbol{e}_i\otimes\boldsymbol{e}_j\otimes\boldsymbol{e}_k\otimes\boldsymbol{e}_l = \boldsymbol{e}_i\otimes\boldsymbol{e}_j\otimes\boldsymbol{e}_j\otimes\boldsymbol{e}_i. \tag{3.14}$$

For an arbitrary second-order tensor $\mathbf{A}$, it can be verified that

$$\mathbb{I}:\mathbf{A} = \mathbf{A}, \quad \bar{\mathbb{I}}:\mathbf{A} = \mathbf{A}^{\mathrm{T}}.$$

The above quantities are needed for the nonlinear finite element formulations to form the element stiffness matrix during the nonlinear iterations.

The anisotropic part of the strain energy function reflects the impact of the fiber orientations on the material behavior. In this work, the following anisotropic strain energy form is adopted:

$$\Psi_{\text{aniso}}(\mathbf{C}) = \Psi_{\text{aniso}}(I_4) = \frac{k_1}{2}\frac{(I_4-1)^2}{I_4^{k_2}}, \tag{3.15}$$

where $k_1 > 0$ is a modulus-like parameter, and $k_2 \in \mathbb{R}$ is a dimensionless parameter that influences the non-linearity of the stress-strain relationship. Particularly, the pseudo-invariant I_4 is defined as

$$I_4 = \mathbf{C}:\mathbf{A} = \mathbf{C}:\boldsymbol{N}\otimes\boldsymbol{N},$$

where $\mathbf{A} = \boldsymbol{N}\otimes\boldsymbol{N}$ is called the structural tensor [35], and $\boldsymbol{N}$ is the unit directional vector reflecting the fiber orientation in the reference configuration. The corresponding 2nd P-K (Piola-Kirchhoff) stress is derived as

$$\mathbf{S}_{\text{aniso}} = 2\frac{\partial \Psi_{\text{aniso}}(I_4)}{\partial \mathbf{C}} = 2\frac{\partial \Psi_{\text{aniso}}(I_4)}{I_4}\frac{I_4}{\partial \mathbf{C}} = k_1\left(\frac{2(I_4-1)}{I_4^{k_2}} - k_2\frac{(I_4-1)^2}{I_4^{k_2+1}}\right)\boldsymbol{N}\otimes\boldsymbol{N}, \tag{3.16}$$

and the corresponding Cauchy stress is

$$\boldsymbol{\sigma}_{\text{aniso}} = J^{-1}\mathbf{F}\mathbf{S}_{\text{aniso}}\mathbf{F}^{\text{T}} = k_1 J^{-1}\left(\frac{2(I_4-1)}{I_4^{k_2}} - k_2\frac{(I_4-1)^2}{I_4^{k_2+1}}\right)\boldsymbol{n}\otimes\boldsymbol{n}, \tag{3.17}$$

where $\boldsymbol{n} = \mathbf{F}\boldsymbol{N}$ represents the fiber orientation in the deformed configuration. It is a widely adopted assumption that fiber can only support tension but not compression. Therefore, the contributions from the anisotropic part can be switched off when $I_4 < 1$, indicating that fiber is under compression [35]. The material elasticity tensor related to the anisotropic part of the strain energy function is derived as:

$$\mathbb{C}_{\text{aniso}} = \alpha\boldsymbol{N}\otimes\boldsymbol{N}\otimes\boldsymbol{N}\otimes\boldsymbol{N}, \tag{3.18}$$

where the scalar coefficient α is defined as

$$\alpha = 2k_1\left(\frac{2}{I_4^{k_2}} - 4k_2\frac{I_4-1}{I_4^{k_2+1}} + k_2(k_2+1)\frac{(I_4-1)^2}{I_4^{k_2+2}}\right). \tag{3.19}$$

The corresponding spatial elasticity tensor related to the anisotropic part of the strain energy function is derived as:

$$\mathbf{c}_{\text{aniso}} = \alpha J^{-1}\boldsymbol{n}\otimes\boldsymbol{n}\otimes\boldsymbol{n}\otimes\boldsymbol{n}. \tag{3.20}$$

It can be verified that when $\mathbf{F} = \mathbf{I}$, representing the undeformed state, $I_4 = 1$, and the anisotropic part of the stress tensor is

$$\mathbf{S}_{\text{aniso}}\Big|_{\mathbf{F}=\mathbf{I}} = \mathbf{0}.$$

The material elasticity tensor is positive definite since

$$\alpha\Big|_{\mathbf{F}=\mathbf{I}} = 4\frac{k_1}{I_4^{k_2}} > 0.$$

In the context of the finite element formulation, the above quantities derived from the hyperelastic constitutive model, including the 2nd-order stress tensor and the 4th-order elasticity tensor, are calculated at each integration point inside each finite element.

3.2 Mixed finite element formulation

In order to effectively enforce the material incompressibility condition, the finite element formulation needs to be carefully designed to avoid the so-called volumetric lock, which causes the material deformation to be overly stiff. In this work, a three-field variational

principle, also known as the mixed $\boldsymbol{u}$-J-p formulation [48,49], is adopted. This variational principle originates from the Hu-Washizu principle [50, 51] and is well documented in several textbooks [43,52]. In this work, according to the three-field variational principle, let $\boldsymbol{\Xi} = \{\boldsymbol{u}, \hat{p}, \hat{J}\}$ be the set of the primary unknowns, in which $\boldsymbol{u}$ represents the displacement field, $\hat{J}$ is a kinematic variable entering the formulation as a constraint on $J = \det\mathbf{F}$, and $\hat{p}$ is the corresponding Lagrange multiplier or pressure. The total potential energy Π of the material is composed of the internal energy Π_{int} and the external energy Π_{ext},

$$\Pi(\boldsymbol{\Xi}) = \Pi_{\text{int}}(\boldsymbol{\Xi}) - \Pi_{\text{ext}}(\boldsymbol{u}). \tag{3.21}$$

The internal energy Π_{int} can be expressed as

$$\Pi_{\text{int}}(\boldsymbol{\Xi}) = \int_{\Omega_0} \left[U(\hat{J}) + \Psi_{\text{iso}}(\bar{\mathbf{C}}) + \Psi_{\text{aniso}}(\mathbf{C}) + \hat{p}(J(\boldsymbol{u}) - \hat{J}) \right] \mathrm{d}V, \tag{3.22}$$

where the volumetric strain energy $U(\hat{J})$ takes the form shown in Eq. (3.2), the isotropic strain energy caused by the shape change $\Psi_{\text{iso}}(\bar{\mathbf{C}})$ takes the form shown in Eq. (3.3), and the anisotropic strain energy $\Psi_{\text{aniso}}(\mathbf{C})$ takes the form shown in Eq. (3.15). The external energy Π_{ext} can be expressed as

$$\Pi_{\text{ext}}(\boldsymbol{u}) = \int_{\Omega_0} \boldsymbol{f}_0 \cdot \boldsymbol{u} \, \mathrm{d}V + \int_{\partial\Omega_{0\boldsymbol{t}}} \bar{\boldsymbol{T}} \cdot \boldsymbol{u} \, \mathrm{d}A, \tag{3.23}$$

where the integral domain Ω_0 represents the space occupied by the material in the reference configuration, $\boldsymbol{f}_0$ is the body force in the reference configuration, and $\bar{\boldsymbol{T}}$ denotes the prescribed first Piola-Kirchhoff traction acting on an infinitesimal area $\mathrm{d}A$ in the reference configuration.

The stationary of the total potential energy can be written as

$$\mathcal{D}_{\delta\boldsymbol{\Xi}}\Pi(\boldsymbol{\Xi}) = \mathcal{D}_{\delta\boldsymbol{u}}\Pi(\boldsymbol{\Xi}) + \mathcal{D}_{\delta\hat{p}}\Pi(\boldsymbol{\Xi}) + \mathcal{D}_{\delta\hat{J}}\Pi(\boldsymbol{\Xi}) = 0, \tag{3.24}$$

for all virtual displacements $\delta\boldsymbol{u} \in H^{(1)}(\Omega)$ satisfying the Dirichlet boundary condition $\delta\boldsymbol{u} = \mathbf{0}$ on $\partial\Omega_{\boldsymbol{u}}$, and all virtual pressure $\delta\hat{p} \in L^2(\Omega)$ and virtual dilatation $\delta\hat{J} \in L^2(\Omega)$. In the above equation, $\mathcal{D}_{\delta(\cdot)}\Pi(\boldsymbol{\Xi})$ represents the directional derivative of the energy functional $\Pi(\boldsymbol{\Xi})$ with respect to the unknown fields. For instance,

$$\mathcal{D}_{\delta\boldsymbol{u}}\Pi(\boldsymbol{\Xi}) = \left.\frac{\mathrm{d}}{\mathrm{d}\epsilon}\right|_{\epsilon=0} \left[\Pi(\boldsymbol{u} + \epsilon\delta\boldsymbol{u},\, \hat{p},\, \hat{J}) \right].$$

Specifically,

$$\begin{aligned} \mathcal{D}_{\delta\boldsymbol{u}}\Pi(\boldsymbol{\Xi}) &= \mathcal{D}_{\delta\boldsymbol{u}}\Pi_{\text{int}}(\boldsymbol{\Xi}) - \mathcal{D}_{\delta\boldsymbol{u}}\Pi_{\text{ext}}(\boldsymbol{u}) \\ &= \int_{\Omega_0} [\mathcal{D}_{\delta\boldsymbol{u}}\Psi_{\text{iso}}(\bar{\mathbf{C}}) + \mathcal{D}_{\delta\boldsymbol{u}}\Psi_{\text{aniso}}(\mathbf{C}) + \mathcal{D}_{\delta\boldsymbol{u}}J(\boldsymbol{u})\hat{p}] \, \mathrm{d}V \\ &\quad - \int_{\Omega_0} \boldsymbol{f}_0 \cdot \delta\boldsymbol{u} \, \mathrm{d}V - \int_{\partial\Omega_{0\boldsymbol{t}}} \bar{\boldsymbol{T}} \cdot \delta\boldsymbol{u} \, \mathrm{d}A, \end{aligned} \tag{3.25}$$

$$\mathcal{D}_{\delta\hat{p}}\Pi(\boldsymbol{\Xi}) = \mathcal{D}_{\delta\hat{p}}\Pi_{\text{int}}(\boldsymbol{\Xi}) = \int_{\Omega_0} \delta\hat{p}(J(\boldsymbol{u}) - \hat{J})\,\mathrm{d}V, \tag{3.26}$$

and

$$\mathcal{D}_{\delta\hat{J}}\Pi(\boldsymbol{\Xi}) = \mathcal{D}_{\delta\hat{J}}\Pi_{\text{int}}(\boldsymbol{\Xi}) = \int_{\Omega_0} \delta\hat{J}\left(\frac{\mathrm{d}U(\hat{J})}{\mathrm{d}\hat{J}} - \hat{p}\right)\mathrm{d}V. \tag{3.27}$$

In the first variation of the internal energy with respect to the displacement field $\mathcal{D}_{\delta\boldsymbol{u}}\Pi_{\text{int}}(\boldsymbol{\Xi})$ shown in Eq. (3.25),

$$\mathcal{D}_{\delta\boldsymbol{u}}\Psi_{\text{iso}}(\bar{\mathbf{C}}) = \delta\Psi_{\text{iso}}(\bar{\mathbf{C}}) = \frac{\partial\Psi_{\text{iso}}(\bar{\mathbf{C}})}{\partial\mathbf{C}} : \delta\mathbf{C} = \mathbf{S}_{\text{iso}} : \delta\mathbf{E} = J\text{grad}\delta\boldsymbol{u} : \boldsymbol{\sigma}_{\text{iso}},$$

$$\mathcal{D}_{\delta\boldsymbol{u}}\Psi_{\text{aniso}}(\mathbf{C}) = \delta\Psi_{\text{aniso}}(\mathbf{C}) = \frac{\partial\Psi_{\text{aniso}}(\mathbf{C})}{\partial\mathbf{C}} : \delta\mathbf{C} = \mathbf{S}_{\text{aniso}} : \delta\mathbf{E} = J\text{grad}\delta\boldsymbol{u} : \boldsymbol{\sigma}_{\text{aniso}},$$

and

$$\mathcal{D}_{\delta\boldsymbol{u}}J(\boldsymbol{u})\hat{p} = \delta J(\boldsymbol{u})\hat{p} = \hat{p}J\text{div}\delta\boldsymbol{u} = \text{grad}\delta\boldsymbol{u} : (\hat{p}J\mathbf{I}),$$

where $\boldsymbol{\sigma}_{\text{iso}}$ and $\boldsymbol{\sigma}_{\text{aniso}}$ are defined in Eqs. (3.7) and (3.17).

From the three-field variational principle shown in Eqs. (3.24) to (3.25), the following Euler-Lagrange equations can be recovered:

$$\begin{cases} \text{div}\boldsymbol{\sigma} + \boldsymbol{f} = \mathbf{0} \quad \text{in} \quad \Omega, \\ J(\boldsymbol{u}) = \hat{J} \quad \text{in} \quad \Omega, \\ \dfrac{\mathrm{d}U(\hat{J})}{\mathrm{d}\hat{J}} = \hat{p} \quad \text{in} \quad \Omega, \\ \boldsymbol{\sigma}\boldsymbol{n} = \bar{\boldsymbol{t}} \quad \text{on} \quad \partial\Omega_{\boldsymbol{t}}, \end{cases}$$

where $\boldsymbol{f} = J^{-1}\boldsymbol{f}_0$ is the body force in the deformed configuration Ω, and the last equation $\boldsymbol{\sigma}\boldsymbol{n} = \bar{\boldsymbol{t}}$ represents the Neumann boundary condition. Notice that the Cauchy stress $\boldsymbol{\sigma}$ in the above Euler-Lagrange equations represents the total stress, which includes the contribute from the Lagrange multiplier (pressure) , that is,

$$\boldsymbol{\sigma} = \hat{p}\mathbf{I} + \boldsymbol{\sigma}_{\text{iso}} + \boldsymbol{\sigma}_{\text{aniso}}.$$

In order to achieve the stationary of the total potential energy shown in Eq. (3.24), the following nonlinear system needs to be solved:

$$\begin{cases} \mathcal{D}_{\delta\boldsymbol{u}}\Pi(\boldsymbol{\Xi}) = \mathcal{D}_{\delta\boldsymbol{u}}\Pi(\boldsymbol{u}, \hat{p}, \hat{J}) = 0, \\ \mathcal{D}_{\delta\hat{p}}\Pi(\boldsymbol{\Xi}) = \mathcal{D}_{\delta\hat{p}}\Pi(\boldsymbol{u}, \hat{p}, \hat{J}) = 0, \\ \mathcal{D}_{\delta\hat{J}}\Pi(\boldsymbol{\Xi}) = \mathcal{D}_{\delta\hat{J}}\Pi(\boldsymbol{u}, \hat{p}, \hat{J}) = 0. \end{cases}$$

For this purpose, the Newton-Raphson iterations are adopted. During a typical loading step, assume that the solution at the beginning of the i-th iteration $\boldsymbol{\Xi}^{(i)} = \left\{\boldsymbol{u}^{(i)}, \hat{p}^{(i)}, \hat{J}^{(i)}\right\}$ is known, the goal is to solve the solution increment $d\,\boldsymbol{\Xi}^{(i)} = \left\{d\boldsymbol{u}^{(i)}, d\hat{p}^{(i)}, d\hat{J}^{(i)}\right\}$ so that at the end of the current iteration, $\boldsymbol{\Xi}^{(i+1)} = \boldsymbol{\Xi}^{(i)} + d\,\boldsymbol{\Xi}^{(i)}$. During the i-th iteration, the linearized system can be expressed as

$$\begin{cases} \mathcal{D}_{\delta\boldsymbol{u}}\Pi(\boldsymbol{\Xi}^{(i+1)}) = \mathcal{D}_{\delta\boldsymbol{u}}\Pi(\boldsymbol{\Xi}^{(i)}) + \mathcal{D}^2_{\delta\boldsymbol{u},\Delta\boldsymbol{u}}\Pi(\boldsymbol{\Xi}^{(i)}) \cdot d\boldsymbol{u}^{(i)} \\ \qquad\qquad + \mathcal{D}^2_{\delta\boldsymbol{u},\Delta\hat{p}}\Pi(\boldsymbol{\Xi}^{(i)})d\hat{p}^{(i)} + \mathcal{D}^2_{\delta\boldsymbol{u},\Delta\hat{J}}\Pi(\boldsymbol{\Xi}^{(i)})d\hat{J}^{(i)} = 0, \\ \mathcal{D}_{\delta\hat{p}}\Pi(\boldsymbol{\Xi}^{(i+1)}) = \mathcal{D}_{\delta\hat{p}}\Pi(\boldsymbol{\Xi}^{(i)}) + \mathcal{D}^2_{\delta\hat{p},\Delta\boldsymbol{u}}\Pi(\boldsymbol{\Xi}^{(i)}) \cdot d\boldsymbol{u}^{(i)} \\ \qquad\qquad + \mathcal{D}^2_{\delta\hat{p},\Delta\hat{p}}\Pi(\boldsymbol{\Xi}^{(i)})d\hat{p}^{(i)} + \mathcal{D}^2_{\delta\hat{p},\Delta\hat{J}}\Pi(\boldsymbol{\Xi}^{(i)})d\hat{J}^{(i)} = 0, \\ \mathcal{D}_{\delta\hat{J}}\Pi(\boldsymbol{\Xi}^{(i+1)}) = \mathcal{D}_{\delta\hat{J}}\Pi(\boldsymbol{\Xi}^{(i)}) + \mathcal{D}^2_{\delta\hat{J},\Delta\boldsymbol{u}}\Pi(\boldsymbol{\Xi}^{(i)}) \cdot d\boldsymbol{u}^{(i)} \\ \qquad\qquad + \mathcal{D}^2_{\delta\hat{J},\Delta\hat{p}}\Pi(\boldsymbol{\Xi}^{(i)})d\hat{p}^{(i)} + \mathcal{D}^2_{\delta\hat{J},\Delta\hat{J}}\Pi(\boldsymbol{\Xi}^{(i)})d\hat{J}^{(i)} = 0, \end{cases} \tag{3.28}$$

or the equivalent matrix form

$$\begin{bmatrix} \mathcal{D}^2_{\delta\boldsymbol{u},\Delta\boldsymbol{u}}\Pi(\boldsymbol{\Xi}^{(i)}) & \mathcal{D}^2_{\delta\boldsymbol{u},\Delta\hat{p}}\Pi(\boldsymbol{\Xi}^{(i)}) & \mathcal{D}^2_{\delta\boldsymbol{u},\Delta\hat{J}}\Pi(\boldsymbol{\Xi}^{(i)}) \\ \mathcal{D}^2_{\delta\hat{p},\Delta\boldsymbol{u}}\Pi(\boldsymbol{\Xi}^{(i)}) & \mathcal{D}^2_{\delta\hat{p},\Delta\hat{p}}\Pi(\boldsymbol{\Xi}^{(i)}) & \mathcal{D}^2_{\delta\hat{p},\Delta\hat{J}}\Pi(\boldsymbol{\Xi}^{(i)}) \\ \mathcal{D}^2_{\delta\hat{J},\Delta\boldsymbol{u}}\Pi(\boldsymbol{\Xi}^{(i)}) & \mathcal{D}^2_{\delta\hat{J},\Delta\hat{p}}\Pi(\boldsymbol{\Xi}^{(i)}) & \mathcal{D}^2_{\delta\hat{J},\Delta\hat{J}}\Pi(\boldsymbol{\Xi}^{(i)}) \end{bmatrix} \begin{bmatrix} d\boldsymbol{u}^{(i)} \\ d\hat{p}^{(i)} \\ d\hat{J}^{(i)} \end{bmatrix} = \begin{bmatrix} -\mathcal{D}_{\delta\boldsymbol{u}}\Pi(\boldsymbol{\Xi}^{(i)}) \\ -\mathcal{D}_{\delta\hat{p}}\Pi(\boldsymbol{\Xi}^{(i)}) \\ -\mathcal{D}_{\delta\hat{J}}\Pi(\boldsymbol{\Xi}^{(i)}) \end{bmatrix}. \tag{3.29}$$

In the above linear system, each entry in the tangent matrix can be expressed as follows:

$$\mathcal{D}^2_{\delta\boldsymbol{u},\Delta\hat{p}}\Pi(\boldsymbol{\Xi}) = \int_{\Omega_0} J\mathrm{div}\delta\boldsymbol{u}\Delta\hat{p}\,\mathrm{d}V,$$

$$\mathcal{D}^2_{\delta\hat{p},\Delta\boldsymbol{u}}\Pi(\boldsymbol{\Xi}) = \int_{\Omega_0} J\mathrm{div}\Delta\boldsymbol{u}\delta\hat{p}\,\mathrm{d}V,$$

$$\mathcal{D}^2_{\delta\hat{p},\Delta\hat{J}}\Pi(\boldsymbol{\Xi}) = -\int_{\Omega_0} \delta\hat{p}\Delta\hat{J}\,\mathrm{d}V,$$

$$\mathcal{D}^2_{\delta\hat{J},\Delta\hat{p}}\Pi(\boldsymbol{\Xi}) = -\int_{\Omega_0} \Delta\hat{p}\delta\hat{J}\,\mathrm{d}V,$$

$$\mathcal{D}^2_{\delta\hat{J},\Delta\hat{J}}\Pi(\boldsymbol{\Xi}) = \int_{\Omega_0} \frac{\mathrm{d}^2U(\hat{J})}{\mathrm{d}\hat{J}^2}\Delta\hat{J}\delta\hat{J}\,\mathrm{d}V,$$

$$\mathcal{D}^2_{\delta\boldsymbol{u},\Delta\hat{J}}\Pi(\boldsymbol{\Xi}) = \mathbf{0}, \quad \mathcal{D}^2_{\delta\hat{J},\Delta\boldsymbol{u}}\Pi(\boldsymbol{\Xi}) = \mathbf{0}, \quad \mathcal{D}^2_{\delta\hat{p},\Delta\hat{p}}\Pi(\boldsymbol{\Xi}) = \mathbf{0},$$

and

$$\begin{aligned}\mathcal{D}^2_{\delta\boldsymbol{u},\Delta\boldsymbol{u}}\Pi(\boldsymbol{\Xi}) &= \int_{\Omega_0}\left[\mathcal{D}^2_{\delta\boldsymbol{u},\Delta\boldsymbol{u}}\Psi_{\text{iso}}(\bar{\mathbf{C}}) + \mathcal{D}^2_{\delta\boldsymbol{u},\Delta\boldsymbol{u}}\Psi_{\text{aniso}}(\mathbf{C}) + \mathcal{D}^2_{\delta\boldsymbol{u},\Delta\boldsymbol{u}}J(\boldsymbol{u})\hat{p}\right]\mathrm{d}V \\ &= \int_{\Omega_0}\mathcal{D}_{\Delta\boldsymbol{u}}\left[\mathrm{grad}\delta\boldsymbol{u} : (\hat{p}J\mathbf{I} + J\boldsymbol{\sigma}_{\text{iso}} + J\boldsymbol{\sigma}_{\text{aniso}})\right]\mathrm{d}V \\ &= \int_{\Omega_0}\mathrm{grad}\delta\boldsymbol{u} : [\mathrm{grad}\Delta\boldsymbol{u}(\hat{p}J\mathbf{I} + J\boldsymbol{\sigma}_{\text{iso}} + J\boldsymbol{\sigma}_{\text{aniso}})]\,\mathrm{d}V \\ &+ \int_{\Omega_0}\mathrm{grad}\delta\boldsymbol{u} : \left[\hat{p}J\mathbf{I}\otimes\mathbf{I} - \hat{p}J(\mathbb{I}+\bar{\mathbb{I}}) + J\mathbf{c}_{\text{iso}} + J\mathbf{c}_{\text{aniso}}\right] : \mathrm{grad}\Delta\boldsymbol{u}\,\mathrm{d}V,\end{aligned}$$

where the spatial elasticity tensors $\mathbf{c}_{\text{iso}}$ and $\mathbf{c}_{\text{aniso}}$ are shown in Eqs. (3.11) and (3.20).

The above finite element approach based on the so-called $\boldsymbol{u}$-J-p formulation is flexible since it can adopt different combinations of the finite element spaces for the primary unknown fields, including the displacement field $\boldsymbol{u}$, the kinematic field $\hat{J}$ for the constraint $J = \det\mathbf{F}$, and the corresponding Lagrange multiplier field $\hat{p}$. In order to avoid the so-called volumetric locking, which is manifested as overly stiff material responses, the finite element spaces for the above three fields have to be carefully selected. In the mixed finite element formulation, the finite element spaces should satisfy the famous Ladyzhenskaya-Babuška-Brezzi (LBB) condition [53, 54], which is also known as the inf-sup condition. It has been widely demonstrated that the following combination of the finite element spaces, $\mathrm{Q}_n \times \mathrm{DGP}_{n-1} \times \mathrm{DGP}_{n-1}$, could circumvent the volumetric locking issue for incompressible materials. In this combination of the finite element spaces, Q_n represents the finite elements of continuous piece-wise Lagrange polynomials of degree n, therefore, ensuring the continuity of the displacement field across element boundaries. On the other hand, DGP_{n-1} represents the finite elements of discontinuous Legendre polynomials of degree $n-1$, which implements the complete polynomial spaces. It is worth pointing out that when $n = 1$, $\mathrm{Q}_1 \times \mathrm{DGP}_0 \times \mathrm{DGP}_0$ does not actually satisfy the LBB (inf-sup) condition. However, in practice, this element is still widely used due to its good convergence behavior. For more detailed discussions about discontinuous pressure elements, see [55].

Let $\boldsymbol{N}_{\boldsymbol{u}_A}$ represent the vector-valued shape function for the displacement field $\boldsymbol{u}$ at node A, $N_{\hat{J}_A}$ represent the scalar-valued shape function for the kinematic field $\hat{J}$ at node A, and $N_{\hat{p}_A}$ represent the scalar-valued shape function for the Lagrange multiplier $\hat{p}$ at node A. Based on the shape functions $\{\boldsymbol{N}_{\boldsymbol{u}_A}, N_{\hat{J}_A}, N_{\hat{p}_A}\}$ and the nodal values $\{\boldsymbol{u}_A, \hat{J}_A, \hat{p}_A\}$, the displacement field, the kinematic field, and the Lagrange multiplier field can be expressed as

$$\boldsymbol{u} = \boldsymbol{N}_{\boldsymbol{u}_A}\boldsymbol{u}_A, \quad \text{and} \quad \hat{J} = N_{\hat{J}_A}\hat{J}_A, \quad \text{and} \quad \hat{p} = N_{\hat{p}_A}\hat{p}_A.$$

Correspondingly, the displacement variation, the kinematic field variation, and the La-

grange multiplier variation can be expressed as

$$\delta \boldsymbol{u} = \boldsymbol{N}_{\boldsymbol{u}_A} \delta \boldsymbol{u}_A, \quad \text{and} \quad \delta \hat{J} = N_{\hat{J}_A} \delta \hat{J}_A, \quad \text{and} \quad \delta \hat{p} = N_{\hat{p}_A} \delta \hat{p}_A,$$

where the Einstein summation is used.

Replacing the first-order and second-order directional derivatives shown in Eq. (3.29) with the corresponding block matrices, the following linear system is obtained during the i-th Newton-Raphson iteration:

$$\begin{bmatrix} \mathbf{K}_{\boldsymbol{u}\boldsymbol{u}} & \mathbf{K}_{\boldsymbol{u}\hat{p}} & \mathbf{0} \\ \mathbf{K}_{\hat{p}\boldsymbol{u}} & \mathbf{0} & \mathbf{K}_{\hat{p}\hat{J}} \\ \mathbf{0} & \mathbf{K}_{\hat{J}\hat{p}} & \mathbf{K}_{\hat{J}\hat{J}} \end{bmatrix} \begin{bmatrix} d\boldsymbol{u}^{(i)} \\ d\hat{p}^{(i)} \\ d\hat{J}^{(i)} \end{bmatrix} = \begin{bmatrix} -\boldsymbol{F}_{\boldsymbol{u}}(\boldsymbol{\Xi}^{(i)}) \\ -F_{\hat{p}}(\boldsymbol{\Xi}^{(i)}) \\ -F_{\hat{J}}(\boldsymbol{\Xi}^{(i)}) \end{bmatrix}.$$

$$\begin{aligned}
\mathbf{K}_{\boldsymbol{u}_A \hat{p}_B} &= \int_{\Omega_0} J \mathrm{div} \boldsymbol{N}_{\boldsymbol{u}_A} N_{\hat{p}_B} \, \mathrm{d}V, \\
\mathbf{K}_{\hat{p}_A \boldsymbol{u}_B} &= \int_{\Omega_0} J \mathrm{div} \boldsymbol{N}_{\boldsymbol{u}_B} N_{\hat{p}_A} \, \mathrm{d}V, \\
\mathbf{K}_{\hat{p}_A \hat{J}_B} &= -\int_{\Omega_0} N_{\hat{p}_A} N_{\hat{J}_B} \, \mathrm{d}V, \\
\mathbf{K}_{\hat{J}_A \hat{p}_B} &= -\int_{\Omega_0} N_{\hat{J}_A} N_{\hat{p}_B} \, \mathrm{d}V, \\
\mathbf{K}_{\hat{J}_A \hat{J}_B} &= \int_{\Omega_0} \frac{\mathrm{d}^2 U(\hat{J})}{\mathrm{d}\hat{J}^2} N_{\hat{J}_A} N_{\hat{J}_B} \, \mathrm{d}V, \\
\mathbf{K}_{\boldsymbol{u}\hat{J}} &= \mathbf{0}, \quad \mathbf{K}_{\hat{J}\boldsymbol{u}} = \mathbf{0}, \quad \mathbf{K}_{\hat{p}\hat{p}} = \mathbf{0},
\end{aligned}$$

and

$$\begin{aligned}
\mathbf{K}_{\boldsymbol{u}_A \boldsymbol{u}_B} = &\int_{\Omega_0} \mathrm{grad} \boldsymbol{N}_{\boldsymbol{u}_A} : [\mathrm{grad} \boldsymbol{N}_{\boldsymbol{u}_B} (\hat{p} J \mathbf{I} + J \boldsymbol{\sigma}_{\mathrm{iso}} + J \boldsymbol{\sigma}_{\mathrm{aniso}})] \, \mathrm{d}V \\
&+ \int_{\Omega_0} \mathrm{grad} \boldsymbol{N}_{\boldsymbol{u}_A} : \left[\hat{p} J \mathbf{I} \otimes \mathbf{I} - \hat{p} J (\mathbb{I} + \bar{\mathbb{I}}) + J \mathbf{c}_{\mathrm{iso}} + J \mathbf{c}_{\mathrm{aniso}} \right] : \mathrm{grad} \boldsymbol{N}_{\boldsymbol{u}_B} \, \mathrm{d}V.
\end{aligned}$$

For the right-hand side in the above linear system,

$$\begin{aligned}
\boldsymbol{F}_{\boldsymbol{u}_A} = &\int_{\Omega_0} J \mathrm{grad} \boldsymbol{N}_{\boldsymbol{u}_A} : [\boldsymbol{\sigma}_{\mathrm{iso}} + \boldsymbol{\sigma}_{\mathrm{aniso}} + \hat{p} \mathbf{I}] \, \mathrm{d}V \\
&- \int_{\Omega_0} \boldsymbol{f}_0 \cdot \boldsymbol{N}_{\boldsymbol{u}_A} \, \mathrm{d}V - \int_{\partial \Omega_{0\boldsymbol{t}}} \bar{\boldsymbol{T}} \cdot \boldsymbol{N}_{\boldsymbol{u}_A} \, \mathrm{d}A, \\
F_{\hat{p}_A} = &\int_{\Omega_0} \delta N_{\hat{p}_A} (J(\boldsymbol{u}) - \hat{J}) \, \mathrm{d}V,
\end{aligned}$$

and

$$F_{\hat{J}_A} = \int_{\Omega_0} N_{\hat{J}_A} \left(\frac{\mathrm{d}U(\hat{J})}{\mathrm{d}\hat{J}} - \hat{p} \right) \mathrm{d}V.$$

Generally speaking, there are two approaches to solve the above linear system containing the block structure. The first approach is to solve the full system monolithically. This approach is easy to implement. However, it does not take advantage of the intrinsic block structure of the linear system. The second approach is to convert the three-field formulation into a modified displacement formulation via the so-called static condensation. Since the unknown fields $\hat{p}$ and $\hat{J}$ are discontinuous across element boundaries, the static condensation can be performed at the element level. That is,

$$\begin{aligned} d\hat{J}^{(i)} &= \mathbf{K}_{\hat{p}\hat{J}}^{-1} \left[F_{\hat{p}}(\boldsymbol{\Xi}^{(i)}) - \mathbf{K}_{\hat{p}\boldsymbol{u}} d\boldsymbol{u}^{(i)} \right] \\ d\hat{p}^{(i)} &= \mathbf{K}_{\hat{J}\hat{p}}^{-1} \left[F_{\hat{J}}(\boldsymbol{\Xi}^{(i)}) - \mathbf{K}_{\hat{J}\hat{J}} d\hat{J}^{(i)} \right] \\ &= \mathbf{K}_{\hat{J}\hat{p}}^{-1} F_{\hat{J}}(\boldsymbol{\Xi}^{(i)}) - \mathbf{K}_{\hat{J}\hat{p}}^{-1} \mathbf{K}_{\hat{J}\hat{J}} \mathbf{K}_{\hat{p}\hat{J}}^{-1} \left[F_{\hat{p}}(\boldsymbol{\Xi}^{(i)}) - \mathbf{K}_{\hat{p}\boldsymbol{u}} d\boldsymbol{u}^{(i)} \right] \end{aligned}$$

Therefore,

$$\begin{aligned} & \mathbf{K}_{\boldsymbol{u}\boldsymbol{u}} d\boldsymbol{u}^{(i)} = \boldsymbol{F}_{\boldsymbol{u}}(\boldsymbol{\Xi}^{(i)}) - \mathbf{K}_{\boldsymbol{u}\hat{p}} d\hat{p}^{(i)} \\ \Rightarrow \quad & \left[\mathbf{K}_{\boldsymbol{u}\boldsymbol{u}} + \mathbf{K}_{\boldsymbol{u}\hat{p}} \mathbf{K}_{\hat{J}\hat{p}}^{-1} \mathbf{K}_{\hat{J}\hat{J}} \mathbf{K}_{\hat{p}\hat{J}}^{-1} \mathbf{K}_{\hat{p}\boldsymbol{u}} \right] d\boldsymbol{u}^{(i)} \\ = \quad & \boldsymbol{F}_{\boldsymbol{u}}(\boldsymbol{\Xi}^{(i)}) - \mathbf{K}_{\boldsymbol{u}\hat{p}} \mathbf{K}_{\hat{J}\hat{p}}^{-1} F_{\hat{J}}(\boldsymbol{\Xi}^{(i)}) + \mathbf{K}_{\boldsymbol{u}\hat{p}} \mathbf{K}_{\hat{J}\hat{p}}^{-1} \mathbf{K}_{\hat{J}\hat{J}} \mathbf{K}_{\hat{p}\hat{J}}^{-1} F_{\hat{p}}(\boldsymbol{\Xi}^{(i)}). \end{aligned}$$

Notice that due to the choices of the finite element spaces for the fields $\hat{p}$ and $\hat{J}$, which are the discontinuous Legendre polynomials, the block matrices $\mathbf{K}_{\hat{p}\hat{J}}$ and $\mathbf{K}_{\hat{J}\hat{p}}$ can both be inverted at the element level.

3.3 Summary

In this chapter, the following two tasks are accomplished. First, the hyperelastic material constitutive model is presented for the modeling of the biomimetic tri-layer scaffold material. Detailed expressions are provided for the 2nd P-K stress tensor and the Cauchy stress tensor as well as the material elasticity tensor and the spatial elasticity tensor. Second, the three-field mixed finite element formulation is presented to enforce the material incompressibility. Detailed element-level expressions, including the element stiffness matrix and the right-hand side vector, are provided. The computational framework based on the above expressions can be implemented in any finite element package or software. In

this work, the numerical implementation is programmed in deal.II [44], which is an open-source C++ finite element library. The proposed computational framework, including the constitutive model and the three-field mixed finite element formulation, will be used in the next chapter to model the mechanical responses of the fabricated tri-layer biomimetic scaffold samples.

Chapter 4

Computational simulations

In this chapter, the mixed finite element formulation is firstly applied to demonstrate its effectiveness in overcoming the volumetric locking of nearly incompressible materials. Then, the proposed computational framework is applied to model the mechanical behavior of the fabricated tri-layer biomimetic scaffold samples. In order to provide more background information, the material fabrication process, microstructure, and experimental tests are briefly described. Even though the material fabrication and experiments are not the focus of this work, these information is important to help readers better understand the tri-layer scaffold material system under investigation. Moreover, the material macroscopic and microscopic structure need to be properly incorporated in the numerical simulations. After that, detailed numerical results using the proposed computational framework are reported and compared with the experimental observations.

4.1 Volumetric locking

In this section, a numerical example is provided to demonstrate the effectiveness of the mixed finite element formulation in overcoming the volumetric locking of nearly incompressible materials. The material is assumed to be isotropic, the strain energy function of which includes the volumetric part shown in Eq. (3.2) and the isotropic part shown in Eq. (3.3). The material parameters include the bulk modulus K and the shear modulus G. Based on the above material parameters, the material Poisson's ratio ν can be expressed as

$$\nu = \frac{3K - 2G}{2(3K + G)} = \frac{3K/G - 2}{2(3K/G + 1)}. \tag{4.1}$$

Obviously, when the ratio between K and G approaches infinity, the material becomes incompressible. That is,

$$\lim_{K/G\to\infty} \nu = \lim_{K/G\to\infty} \frac{3K/G - 2}{2(3K/G + 1)} = 0.5. \tag{4.2}$$

In this numerical example, a unit cube deforms under the impact of gravity (the downward body force). The top surface of the unit cube is fixed in all the three directions as the adopted Dirichlet boundary condition. All the material parameters and geometric dimensions are assumed to be dimensionless, so that the focus is to investigate the impact of the ratio K/G on the numerical results. Two different finite element formulations are used. The first approach uses the common displacement-based Q_1 element (piece-wise linear Lagrange polynomial), also known as the tri-linear element. The second approach uses the mixed finite element formulation of $\mathrm{Q}_1 \times \mathrm{DGP}_0 \times \mathrm{DGP}_0$ element as described in Chapter 3.

When the ratio between the bulk modulus K and the shear modulus G is $K/G = 10.0$, Fig. 4.1 compares the downward deformation of the unit cube obtained from the regular displacement-based Q_1 element and the mixed finite element formulation of $\mathrm{Q}_1 \times \mathrm{DGP}_0 \times \mathrm{DGP}_0$ element. In this case, since the material is compressible with the Poisson's ratio of 0.4516, both finite element processes obtain similar results. When the ratio between the bulk modulus K and the shear modulus G increases to $K/G = 1000.0$, the material approaches to be incompressible as the Poisson's ratio is $\nu = 0.4985$. In this case, as shown in Fig. 4.2, the numerical result obtained from the regular displacement-based tri-linear Q_1 element exhibits severely volumetric locking, which is manifested as the overly stiff material response. On the other hand, the mixed finite element formulation using the $\mathrm{Q}_1 \times \mathrm{DGP}_0 \times \mathrm{DGP}_0$ element can still generate correct results even the material becomes nearly incompressible.

Moreover, the mixed finite element formulation can easily accommodate higher-order elements. For instance, Fig. 4.3 reports the kinematic field entering the formulation as a constraint on $J = \det\mathbf{F}$ obtained by using the mixed $\mathrm{Q}_1 \times \mathrm{DGP}_0 \times \mathrm{DGP}_0$ element and the mixed $\mathrm{Q}_2 \times \mathrm{DGP}_1 \times \mathrm{DGP}_1$. Both elements can effectively enforce the material near incompressibility ($J = \det\mathbf{F} \approx 1.0$). However, the kinematic field obtained by using the latter is more smooth since the first-order Legendre polynomial is adopted.

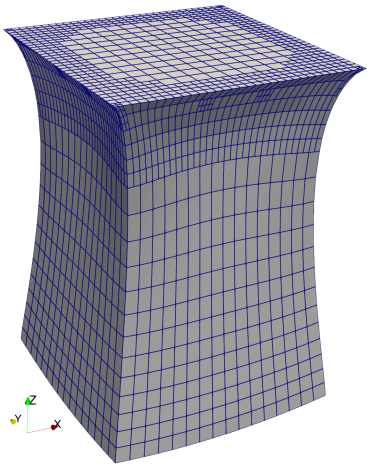

(a) Adaptively refined mesh using Q_1 element

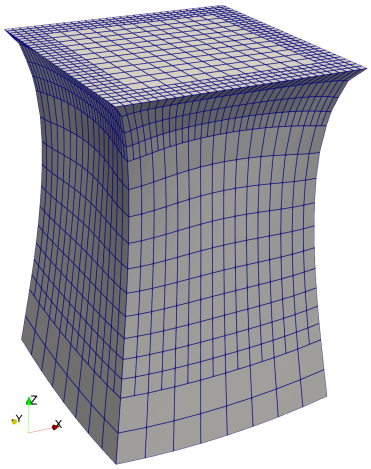

(b) Adaptively refined mesh using mixed $Q_1 \times DGP_0 \times DGP_0$ element

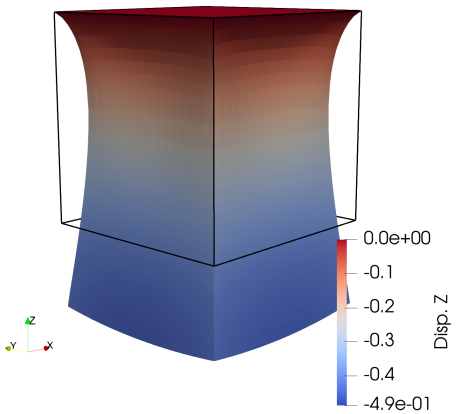

(c) Displacement-based Q_1 element

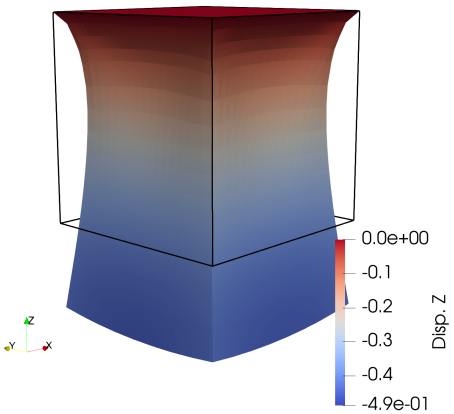

(d) Mixed $Q_1 \times DGP_0 \times DGP_0$ element

Figure 4.1: A unit cube deforms under the downward applied body force (gravity). The ratio between the bulk modulus and the shear modulus is $K/G = 10.0$, such that the material Poisson's ratio ν is 0.4516. In this case, the material is compressible. Therefore, both (a) the tri-linear Q_1 element and (b) the mixed $Q_1 \times DGP_0 \times DGP_0$ element generate similar deformation in the downward direction.

4.2 Tri-layer scaffold fabrication and experiment

The material fabrication and mechanical tests of the tri-layer biomimetic scaffold samples are mainly preformed by the research team of Dr. Xing Zhang at the Chinese Academy of

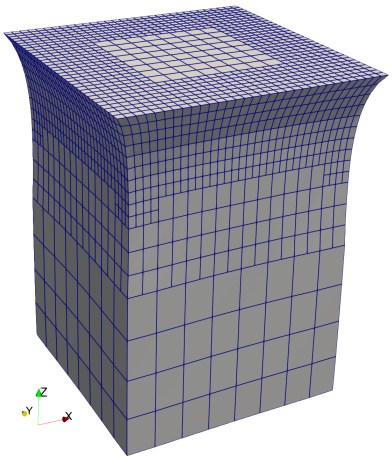

(a) Adaptively refined mesh using Q_1 element

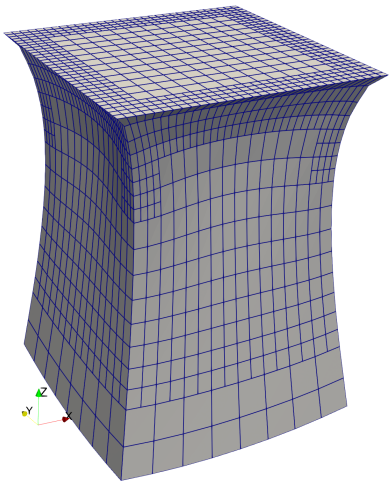

(b) Adaptively refined mesh using mixed $Q_1 \times DGP_0 \times DGP_0$ element

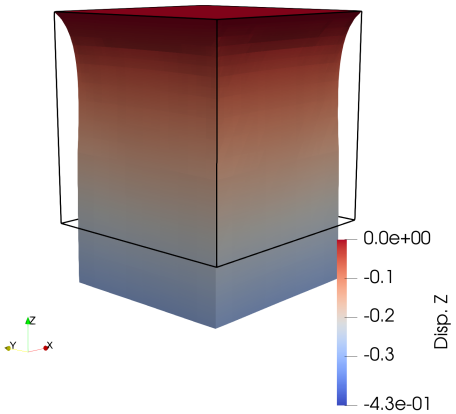

(c) Displacement-based Q_1 element

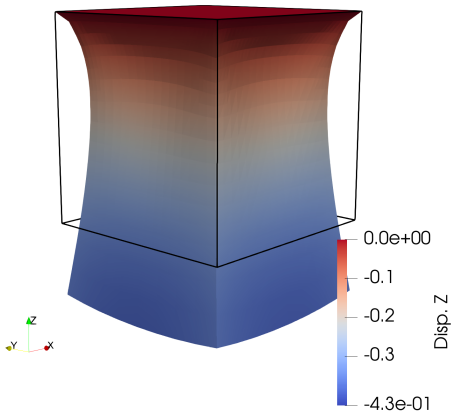

(d) Mixed $Q_1 \times DGP_0 \times DGP_0$ element

Figure 4.2: A unit cube deforms under the downward applied body force (gravity). The ratio between the bulk modulus and the shear modulus is $K/G = 1000.0$, such that the material approaches to be incompressible as the Poisson's ratio ν is 0.4985. In this case, the numerical result obtained from (a) the tri-linear Q_1 element exhibits severely volumetric locking, while (b) the mixed $Q_1 \times DGP_0 \times DGP_0$ element can still generate the correct deformation in the downward direction.

Sciences. This section provides a high-level overview about the experimental work. The material macroscopic and microscopic structures observed during various imaging process will be incorporated into the subsequent numerical simulations. Figure 4.4 shows the

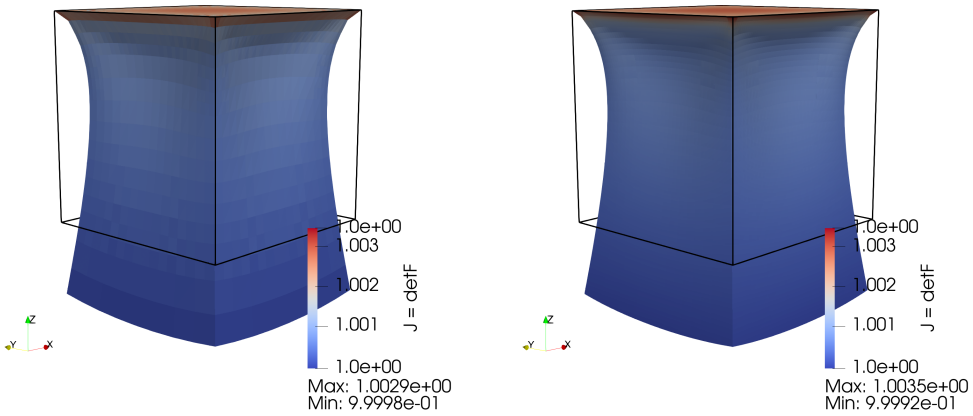

(a) Mixed $Q_1 \times DGP_0 \times DGP_0$ element (b) Mixed $Q_2 \times DGP_1 \times DGP_1$ element

Figure 4.3: A unit cube deforms under the downward applied body force (gravity). The ratio between the bulk modulus and the shear modulus is $K/G = 1000.0$, such that the material approaches to be incompressible as the Poisson's ratio ν is 0.4985. In this case, both (a) the mixed $Q_1 \times DGP_0 \times DGP_0$ element and (b) the mixed $Q_2 \times DGP_1 \times DGP_1$ element can effectively overcome the volumetric locking. Meanwhile, the latter generates a more smooth kinematic field distribution due to the adopted higher-order Legendre polynomial.

schematic of the fabrication process of the biomimetic tri-layer scaffold sample using the electrospinning technology. The scaffold sample includes three layers containing different microstructures. The top layer has a thickness of 60 mm, and the bottom layer has a thickness of 40 mm. Each of these two layers contain a set of highly aligned fibers. The set of fibers inside the top layer is perpendicular to the counterpart contained in the bottom layer. Between the top layer and the bottom layer, these exists a middle layer of 100 mm thickness, which contains a series of honeycomb patterns.

Using the technique of the scanning electron microscope (SEM) imaging, the microstructure of the top layer and the bottom layer is shown in Fig. 4.5. As intended, the fibers in these two layers are highly aligned. Similarly, Fig. 4.6 shows the SEM imaging of the middle layer contained in the tri-layer scaffold material sample. Inside the middle layer, each unit of honeycomb pattern can be approximately divided into three regions, including the center region, the surrounding region, and the hexagon edge region. Figure 4.7 further shows the thickness of different regions in the middle layer of the tri-layer scaffold sample using the confocal laser microscope imaging. This image reveals the dimensions of

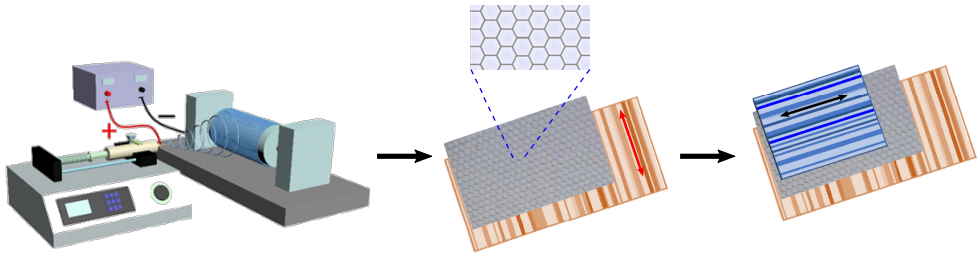

Figure 4.4: Schematic of the fabrication process of the biomimetic tri-layer scaffold sample, which includes the top layer, the bottom layer, and the middle layer. The top layer (60 mm thickness) and the bottom layer (40 mm thickness) contain two sets of mutually orthogonal fibers, while the middle layer (100 mm thickness) contains a set of honeycomb patterns. (Image courtesy of Dr. Xing Zhang, Chinese Academy of Sciences.)

individual region contained in a unit honeycomb cell. Inside a unit honeycomb cell, the diameter of the center region is around 700 μm, the diameter of the region around the center is around 1007 μm, and the width of the hexagon edge is around 208 μm. These geometric dimensions are extremely important for the subsequent numerical simulations.

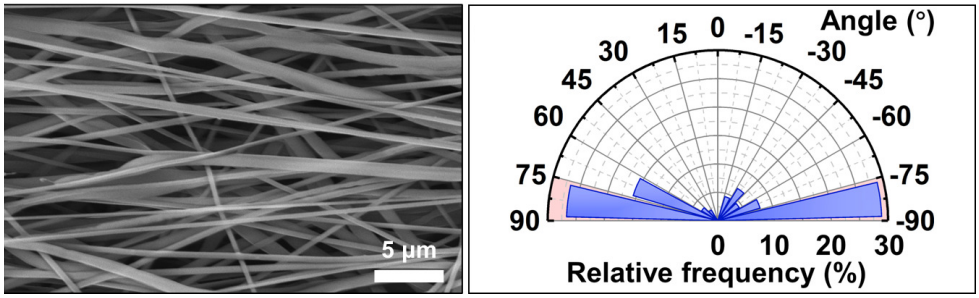

Figure 4.5: Scanning electron microscope (SEM) imaging of the top and bottom layers in the tri-layer scaffold sample. Fibers in these two layers are highly aligned in a fixed direction. (Image courtesy of Dr. Xing Zhang, Chinese Academy of Sciences)

Several mechanical tests are further performed on the fabricated tri-layer scaffold material samples to evaluate the material mechanical properties. First, the mechanical properties of individual layers, including the top layer, the bottom layer, and the middle layer, are tested separately. For instance, Fig. 4.8 shows the mechanical test setup of the middle layer containing the honeycomb patterns. The fabricated middle layer samples are stretched in two orthogonal directions, respectively. The X-direction refers to the direction connecting the two opposite vertices of the hexagon shape. The Y-direction refers to the direction that is perpendicular to the two opposite edges of the hexagon shape. As shown in Fig. 4.8, the middle layer sample exhibits the anisotropic responses and behaves

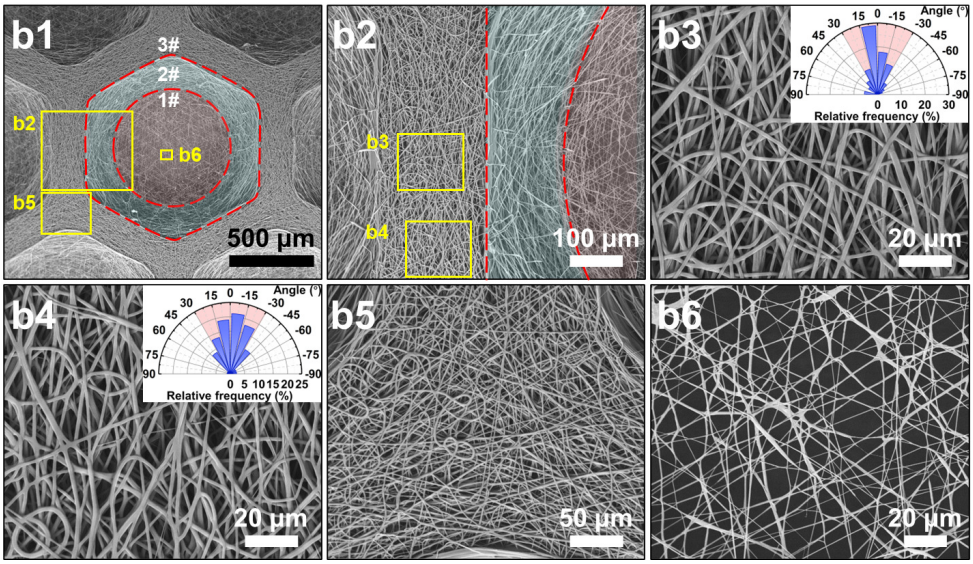

Figure 4.6: Scanning electron microscope (SEM) imaging of the middle layer in the tri-layer scaffold sample. The middle layer contains a series of honeycomb patterns. Each honeycomb unit area can be divided into three regions: the region in the center (1#), the region around the center (2#), and the hexagon edge region (3#). (Image courtesy of Dr. Xing Zhang, Chinese Academy of Sciences)

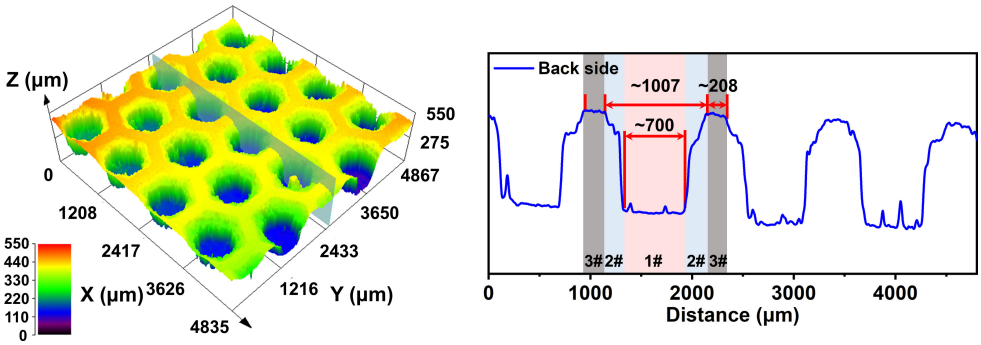

Figure 4.7: Confocal laser microscope imaging that shows the thickness of different regions in the middle layer of the tri-layer scaffold sample. Inside a unit honeycomb area, the diameter of the center region is around 700 μm, the diameter of the region around the center is around 1007 μm, and the width of the hexagon edge is around 208 μm. (Image courtesy of Dr. Xing Zhang, Chinese Academy of Sciences)

differently, depending on the direction of the applied load. When the sample is stretched in the X-direction, the material sample exhibits a more significant transverse deformation than when the sample is stretched in the Y-direction.

After individual layers are tested, the mechanical responses of the entire tri-layer scaf-

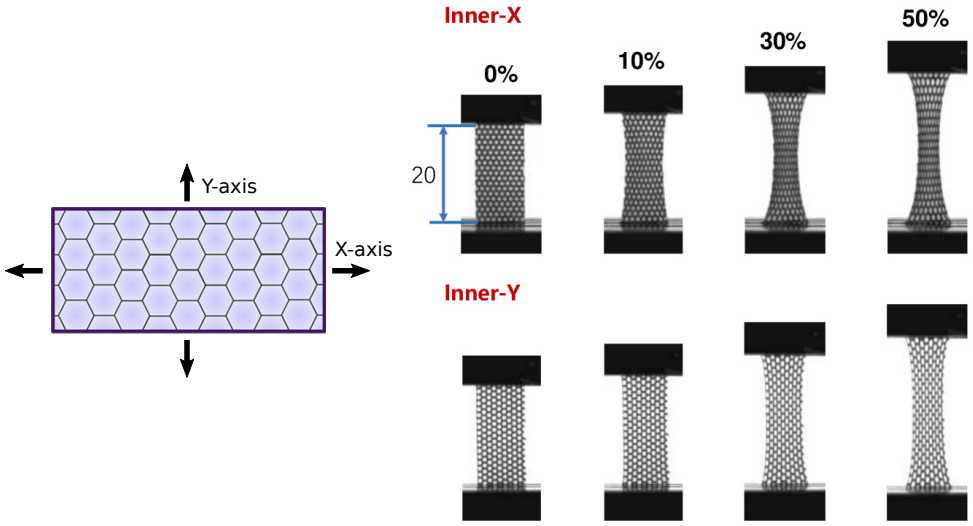

Figure 4.8: Mechanical tests of the middle layer containing the honeycomb patterns. The material sample is stretched along two directions, respectively. The X-direction refers to the direction connecting the two opposite vertices of the hexagon shape. The Y-direction refers to the direction that is perpendicular to the two opposite edges of the hexagon shape. (Image courtesy of Dr. Xing Zhang, Chinese Academy of Sciences)

fold samples are tested, as shown in Fig. 4.9. The objective of these mechanical tests is to verify the anisotropic and nonlinear behavior of the fabricated scaffold sample, with the hope that it can mimic the mechanical behavior of native heart valve tissues, including their anisotropy and nonlinear responses.

4.3 Numerical results

In this section, the computational framework developed in Chapter 3 is applied to model the mechanical behavior of the fabricated tri-layer scaffold sample. The obtained numerical results are further compared with the experimental data and observations.

4.3.1 Top and bottom layers

As shown in Fig. 4.4, the top layer and the bottom layer of the tri-layer biomimetic scaffold sample contain highly aligned fibers that are mutually orthogonal. Their mechanical responses under the uni-axis tension tests are simulated via the proposed computational framework detailed in Chapter 3. Table 4.1 lists the material parameters used for the

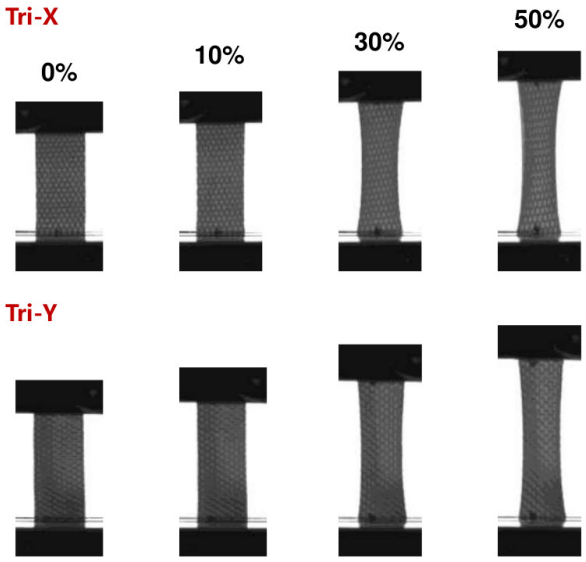

Figure 4.9: Mechanical tests of the tri-layer scaffold sample. The material sample is stretched along two directions, respectively. The X-direction refers to the direction connecting the two opposite vertices of the hexagon shape. The Y-direction refers to the direction that is perpendicular to the two opposite edges of the hexagon shape. (Image courtesy of Dr. Xing Zhang, Chinese Academy of Sciences)

numerical simulation. The meaning of these parameters are explained in Section 3.1. Notice that the ratio between the material bulk modulus K and the shear modulus G is 10^5. This ratio could effectively enforce the material incompressibility condition. Moreover, the only difference between the top layer and the bottom layer regarding the material parameters is the unit directional vector $\boldsymbol{N}$. For the top layer, the fiber orientation is aligned with the loading direction such that the unit direction vector is $\boldsymbol{N} = (1, 0, 0)$. On the other hand, since the fibers inside the bottom layer are perpendicular to the loading direction, the unit directional vector is $\boldsymbol{N} = (0, 1, 0)$.

Table 4.1: Material parameters used for the simulations of the top and bottom layers (K is the bulk modulus, G is the shear modulus, k_1 is the fiber stiffness parameter, k_2 is the fiber nonlinearity parameter, and $\boldsymbol{N}$ is the fiber directional vector).

Test case	K (MPa)	G (MPa)	k_1 (MPa)	k_2	$\boldsymbol{N}$
Top layer	3000.0	0.3	8.5	1.05	(1, 0, 0)
Bottom layer	3000.0	0.3	8.5	1.05	(0, 1, 0)

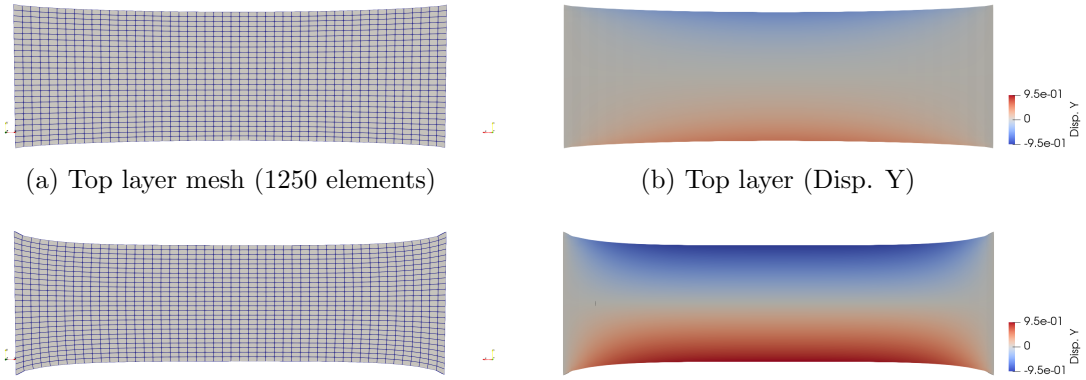

(a) Top layer mesh (1250 elements)

(b) Top layer (Disp. Y)

(c) Bottom layer mesh (1250 elements)

(d) Bottom layer (Disp. Y)

Figure 4.10: Numerical results of the transverse deformation of (a) the top layer sample and (b) the bottom layer sample under the tension test at the stretch ratio $\lambda = 1.5$ (50% strain). The top layer sample contains fibers that are aligned along the loading direction, and the bottom layer sample contains fibers that are aligned perpendicular to the loading direction.

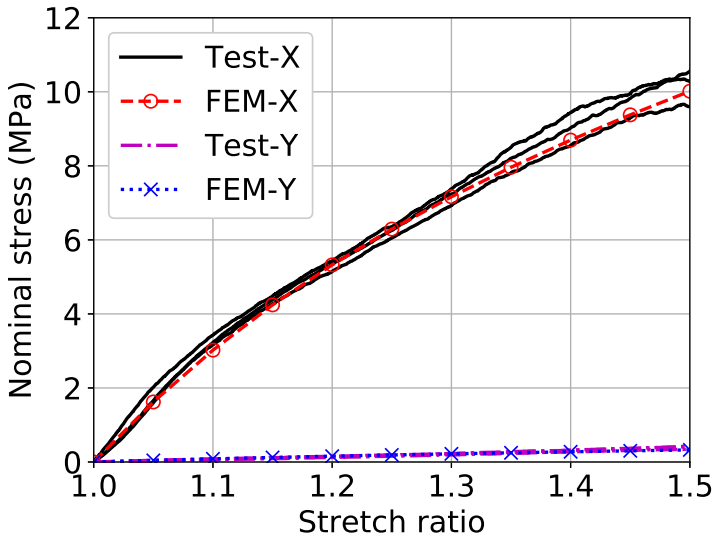

Figure 4.11: Comparisons of the force-displacement relationships of the top layer sample and the bottom layer sample obtained from the numerical simulation (FEM) and the experiment (Test). Since the top layer contains fibers aligned along the loading direction, it is much stiffer than the bottom layer containing fibers perpendicular to the loading direction.

Figure 4.10 show the transverse displacement (disp-y) of the top layer and the bottom layer under the uni-axial loading obtained from the finite element simulations. Figure 4.11

compares the load-displacement relationships of the top and bottom layers obtained from the experimental tests and the finite element simulations. The proposed constitutive model and the three-field mixed finite element method can accurately model the anisotropic behavior of the top and bottom layers.

4.3.2 Honeycomb layer

In the tri-layer biomimetic scaffold sample, these exists a middle layer between the top and bottom layers. The middle layer contains a series of honeycomb patterns, as shown in Figs. 4.4 and 4.6. The proposed finite element modeling technique is used to simulate the mechanical responses of the honeycomb layer in two mutually orthogonal directions. The "X-axis" represents the direction aligned with the diagonal of the hexagon shape in the sample, while the "Y-axis" represents the direction perpendicular to the two opposite edges of the hexagon shape in the sample. Figure 4.12 shows the finite element meshes used for the honeycomb layer, in which different colors represent the fiber orientation angle of the corresponding hexagon edge. For instance, when the honeycomb sample is stretched along the X-axis (diagonal of the hexagon), the corresponding fiber orientation angles are 30°, 90°, and 150°, respectively, for the three pairs of the hexagon edges. Consequently, the unit directional vectors used in the material constitutive model shown in Eq. (3.16) are $\boldsymbol{N} = (\cos 30°, \sin 30°, 0)$, $(\cos 90°, \sin 90°, 0)$, and $(\cos 150°, \sin 150°, 0)$, respectively. When the honeycomb sample is stretched along the "Y-axis" (opposite edges of the hexagon), the corresponding fiber orientation angles are 0°, 60°, and 120°, respectively, for the three pairs of the hexagon edges. Therefore, the unit directional vectors used in the material constitutive model shown in Eq. (3.16) are $\boldsymbol{N} = (\cos 0°, \sin 0°, 0)$, $(\cos 60°, \sin 60°, 0)$, and $(\cos 120°, \sin 120°, 0)$, respectively. These unit directional vectors reflect the preferred direction of the fiber orientations inside the hexagon edges. Additionally, around the hexagon edges, there is also a thin layer of fibers with no preferred direction in the finite element model.

Figures 4.13 and 4.14 show the deformation of the honeycomb layer along the X-axis and Y-axis under the uni-axial tension load at various strain levels. The honeycombe sample along the X-axis (diagonal of the hexagon) has a larger transverse deformation in the width direction than the counterpart of the sample along the Y-axis (opposite edges of the hexagon). Figures 4.15 and 4.16 compare the numerical results and the experimental observations related to the deformed shape of the honeycomb layer at various strain levels. The deformed shapes of the samples between the strain level 0% to 50% match the experimental observations.

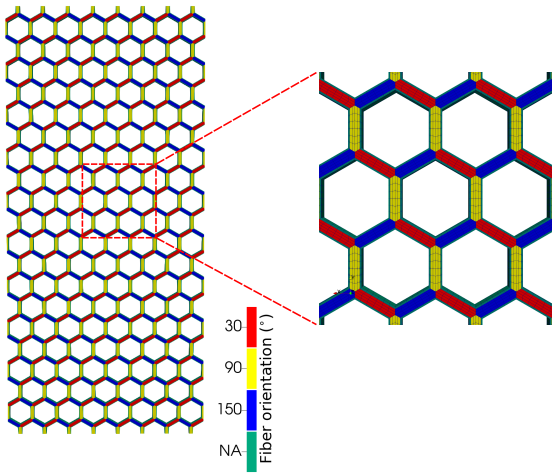

(a) Honeycomb layer (X-axis, 22912 elements)

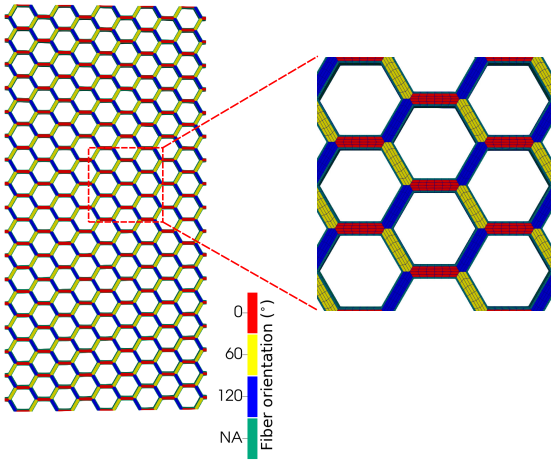

(b) Honeycomb layer (Y-axis, 24208 elements)

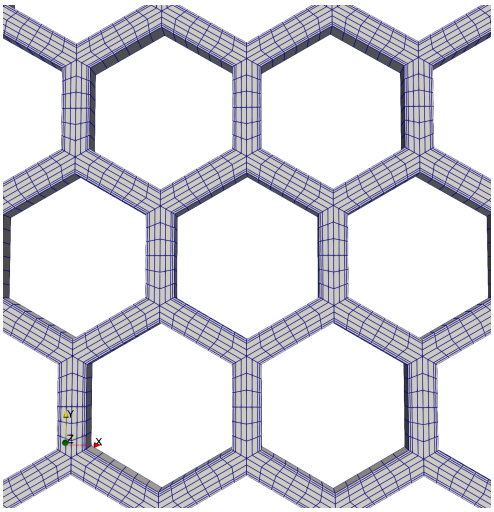

(c) Honeycomb layer mesh (X-axis)

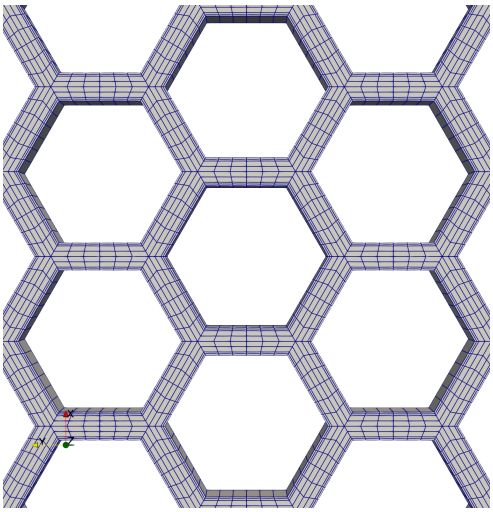

(d) Honeycomb layer mesh (Y-axis)

Figure 4.12: Finite element meshes used for (a) the honeycomb middle layer along the X-axis (diagonal of the hexagon) and (b) the honeycomb intermediate layer along the Y-axis (opposite edges of the hexagon). In the sample along the X-axis (a), the fibers forming the edges of the hexagon have the orientation angles of 30°, 90°, and 150° with respect to the horizontal direction. In the sample along the Y-axis (b), the fibers forming the edges of the hexagon have the orientation angles of 0°, 60°, and 120° with respect to the horizontal direction. Inside each unit hexagon, a thin layer of isotropic material is introduced to mimic the corresponding region observed in the SEM imaging.

Figures 4.17 and 4.18 further report the normal stresses σ_{11} and σ_{22} obtained from the finite element simulations. The geometric pattern of the honeycomb layer has a significant

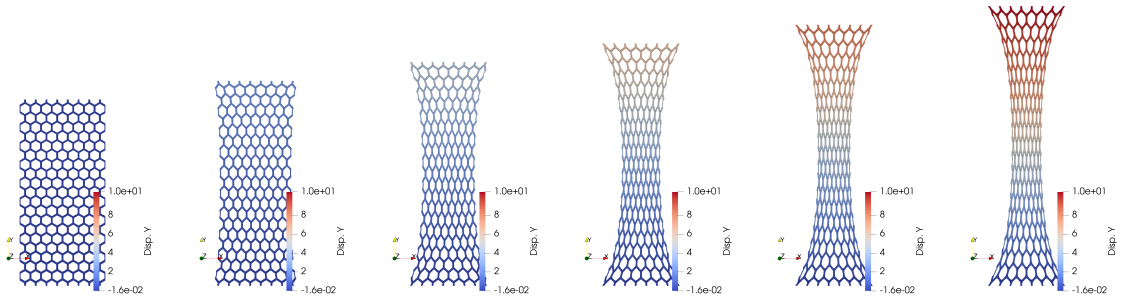

(a) 0% (b) 10% (c) 20% (d) 30% (e) 40% (f) 50%

Figure 4.13: Displacement (unit: mm) along the loading direction for the honeycomb sample (X-axis) at various strain level (0% - 50%) obtained from the finite element simulation.

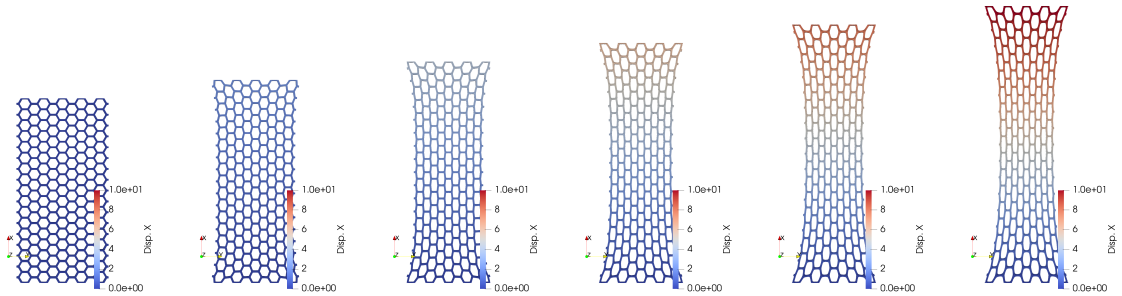

(a) 0% (b) 10% (c) 20% (d) 30% (e) 40% (f) 50%

Figure 4.14: Displacement (unit: mm) along the loading direction for the honeycomb sample (Y-axis) at various strain level (0% - 50%) obtained from the finite element simulation.

influence on the material nonlinear and anisotropic behaviors. When the honeycomb layer is loaded along the diagonal direction (X-axis) of the hexagon pattern, all the hexagons are gradually squeezed, causing a significant deformation in the transverse direction. On the other hand, when the honeycomb layer is loaded perpendicular to the opposite hexagon edges (Y-axis), the hexagon patterns are capable to provide resistance to the transverse deformation, which is manifested as smaller shrinkage of the sample's cross-section.

4.3.3 Tri-layer scaffold

After the top layer, the bottom layer, and the middle honeycomb layer of the tri-layer scaffold material sample are modeled separately, a complete finite element model of the entire tri-layer structure is created, as shown in Fig. 4.19. The top layer has a thickness of 60 mm, the bottom layer has a thickness of 40 mm, and the middle layer has a thickness

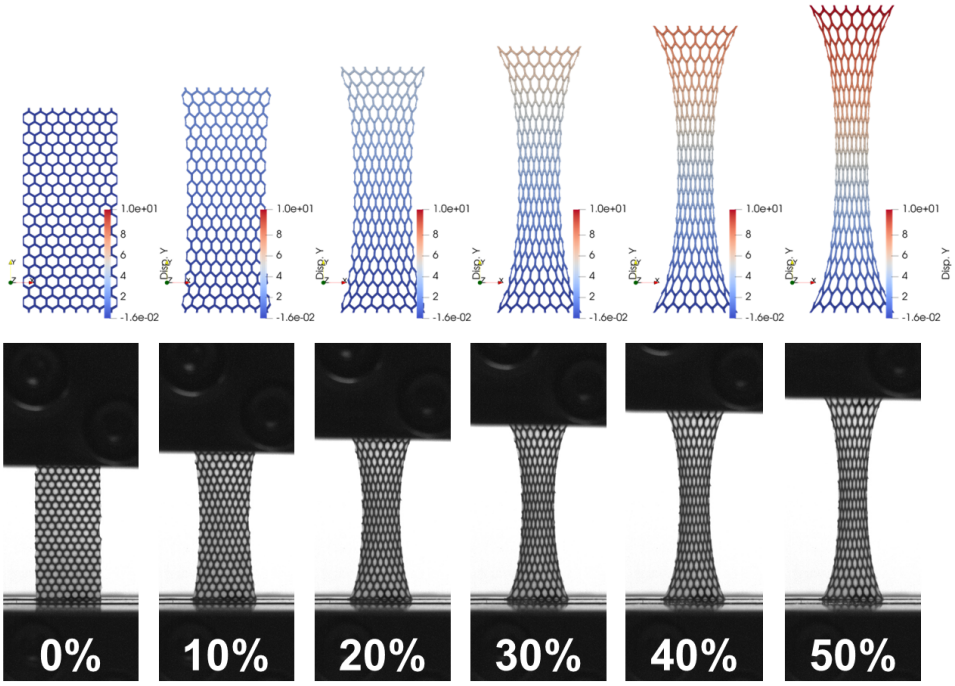

Figure 4.15: Comparison of the middle (honeycomb) layer deformation obtained from the experiment (bottom row) and the finite element simulation (top row) at various strain levels along the X-axis (diagonal of the hexagon).

of 100 mm. These geometric dimensions are consistent with the actual material sample dimensions. Particularly, Fig. 4.19b offers a view of the interior of the tri-layer scaffold material by slicing the finite element model from the center. The honeycomb shape patterns are obvious. During the process of creating the finite element mesh of the entire tri-layer scaffold sample, it is important to ensure that the meshes for the top and bottom layers conform to the middle honeycomb layer. This feature is achieved by creating the three layers of the sample first and then remove the finite elements located inside each hexagon region of the middle layer.

Figures 4.20 and 4.21 show the stress distributions of σ_{11} and σ_{22} when the tri-layer scaffold sample is loaded along the X-axis and Y-axis, respectively. It is obvious that the presence of the middle layer honeycomb shape could significantly impact the stress distribution inside the tri-layer scaffold sample. Moreover, depending the direction along which the external load is applied, the deformed shape and the stress distribution of the tri-layer scaffold sample are significantly different, demonstrating the anisotropy of the material sample.

In order to further validate the effectiveness of the proposed computational framework,

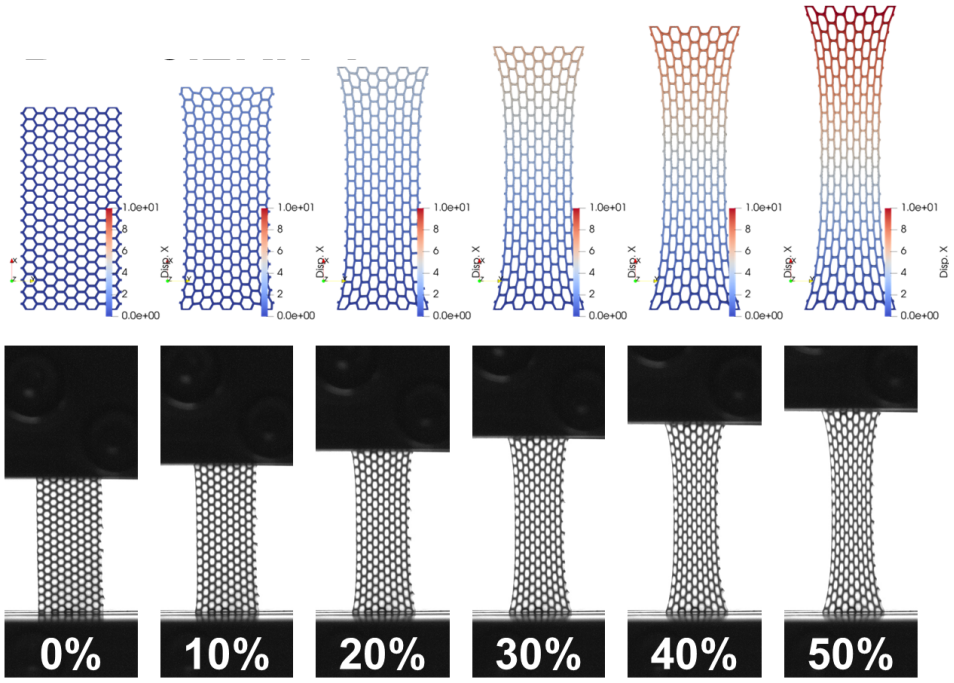

Figure 4.16: Comparison of the middle (honeycomb) layer deformation obtained from the experiment (bottom row) and the finite element simulation (top row) at various strain levels along the Y-axis (opposite edges of the hexagon).

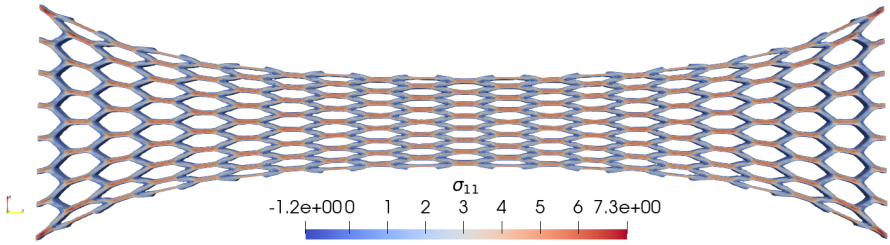

(a) Cauchy stress σ_{11} (X-axis)

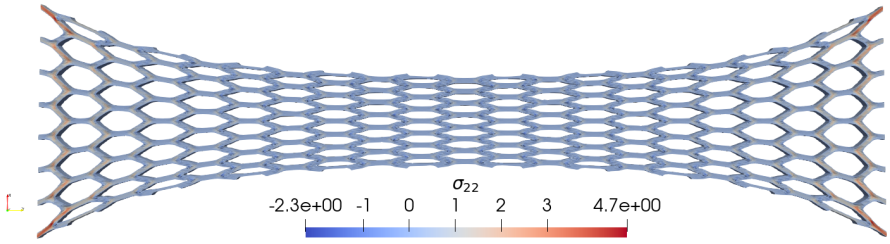

(b) Cauchy stress σ_{22} (X-axis)

Figure 4.17: Cauchy stress (a) σ_{11} and (b) σ_{22} distributions (unit: MPa) inside the honeycomb layer stretched along the X-axis (diagonal of the hexagon) at the 50% strain level.

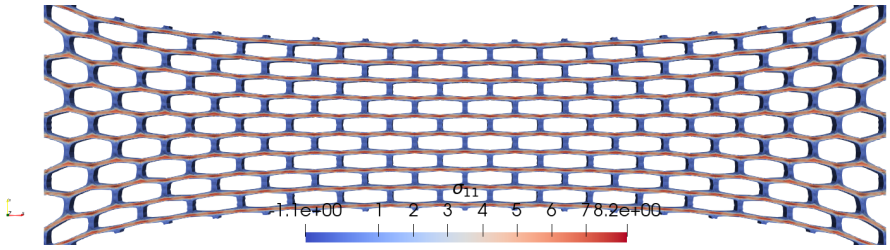

(a) Cauchy stress σ_{11} (Y-axis)

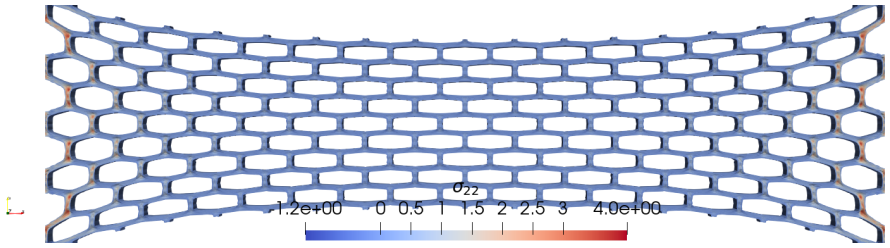

(b) Cauchy stress σ_{22} (Y-axis)

Figure 4.18: Cauchy stress (a) σ_{11} and (b) σ_{22} distributions (unit: MPa) inside the honeycomb layer stretched along the Y-axis (opposite edges of the hexagon) at the 50% strain level.

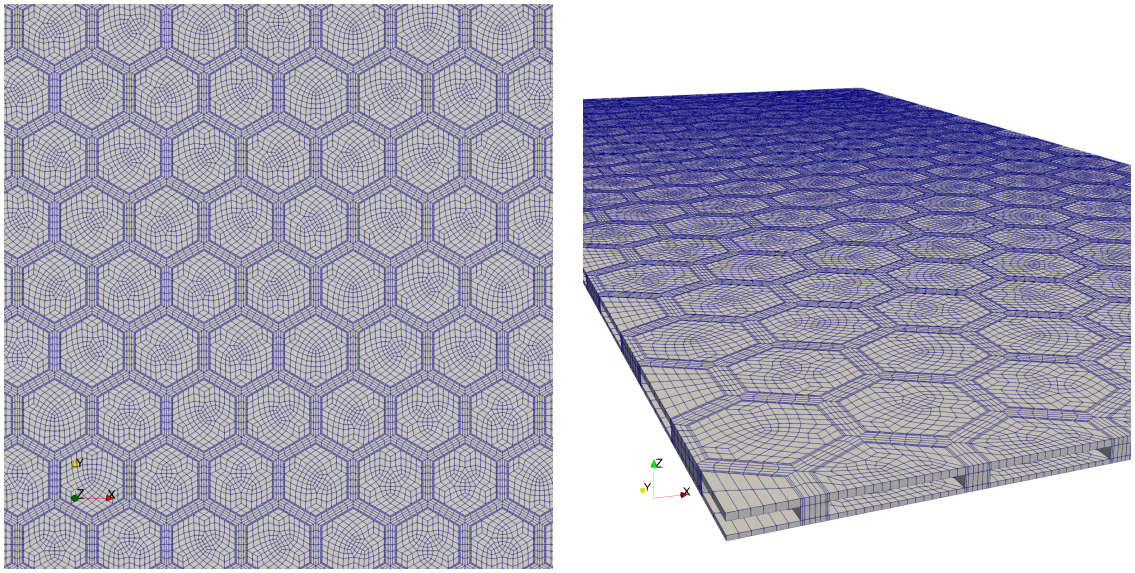

(a) Top view (b) Side view

Figure 4.19: Finite element mesh of the tri-layer scaffold material sample, which contains the top layer, the bottom layer, and the middle layer of the honeycomb patterns. There are 107,568 elements in total.

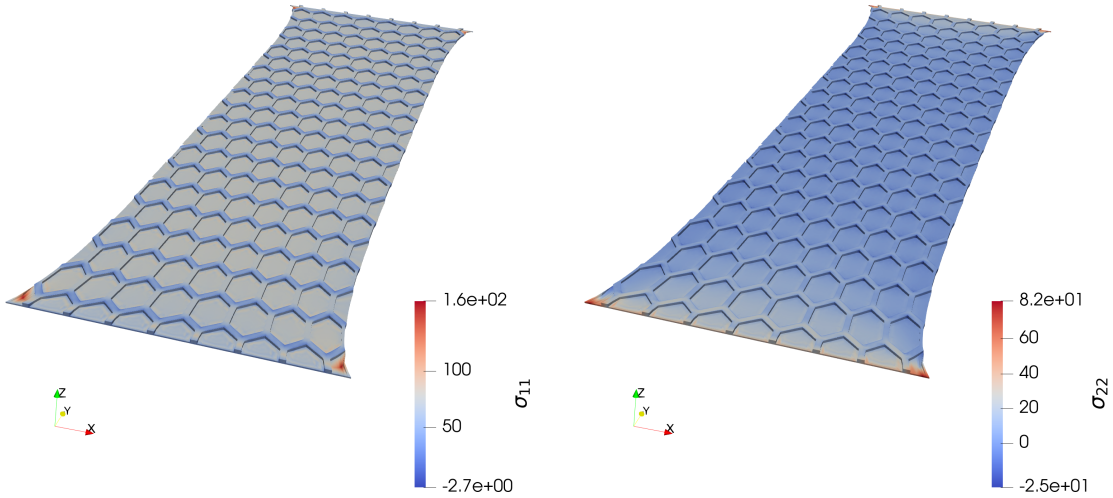

(a) σ_{11} (unit: MPa) (b) σ_{22} (unit: MPa)

Figure 4.20: Finite element simulation results of the stress distribution inside the tri-layer scaffold sample stretched along the X-axis (diagonal of the hexagon).

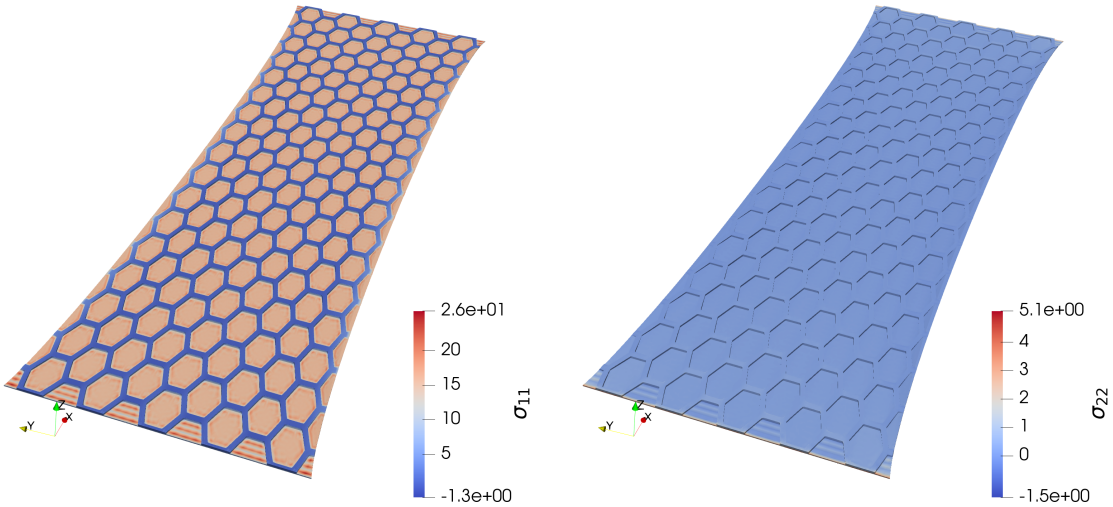

(a) σ_{11} (unit: MPa) (b) σ_{22} (unit: MPa)

Figure 4.21: Finite element simulation results of the stress distribution inside the tri-layer scaffold sample stretched along the Y-axis (opposite edges of the hexagon).

the stress-strain relationships of the entire tri-layer scaffold sample obtained from the experimental tests and the finite element simulations are compared. As shown in Fig. 4.22,

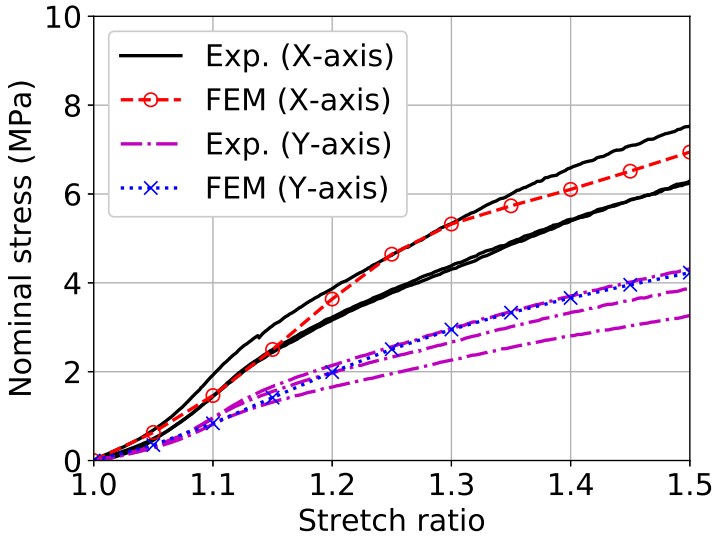

Figure 4.22: Comparisons of the force-displacement relationships of the tri-layer scaffold sample obtained from the numerical simulation (FEM) and the experiment (Exp.). The fabricated tri-layer scaffold sample exhibits anisotropic behavior similar to native heart valve tissues.

the numerical results match the experimental observations in both load directions. More importantly, as indicated in the stress-strain relationship, the fabricated tri-layer scaffold sample has a similar mechanical response compared to native heart valve tissues. In literature, native biological tissues are reported to have a stress-strain relationship that can be divided into three distinctive regions [56–59]: a toe region, a heel region, and a linear region. The toe region exhibits a relatively low elastic modulus, because most collagen fibers are crimped and do not contribute to the material stiffness at small tensile strains. As the strain begins to increase, collagen fibers are gradually straightened, leading to the upward bend of the stress-strain curve in the heel region. The linear region has a larger linear modulus because the majority of collagen fibers are completely straight and contribute to the material stiffness. As shown in Fig. 4.22, the stress-strain of the fabricated tri-layer biomimetic scaffold sample exhibits a similar toe-heel-linear response, indicating that its mechanical properties are similar to the counterparts in native biological tissues. Moreover, the tri-layer sample clearly demonstrates an anisotropic behavior. All of these observations suggest that the fabricated tri-layer material can be used as the scaffold for tissue-engineered heart valves.

4.4 Summary

In this chapter, the proposed constitutive model and the three-field mixed finite element formulation are applied to model the mechanical responses of the fabricated tri-layer biomimetic scaffold samples. The top layer, the bottom layer, and the honeycomb middle layer of the tri-layer sample are first modeled separately. Then, the mechanical response of the entire tri-layer scaffold sample is simulated using the finite element method. The numerical results are further compared with the corresponding experimental observations. Moreover, the impacts of the honeycomb patterns contained in the middle layer of the tri-layer scaffold sample on the material deformation and the stress distributions are quantified in detail. It is demonstrated that the proposed numerical approach can accurately simulate the nonlinear and anisotropic mechanical responses of the fabricated tri-layer scaffold material sample. Particularly, the proposed constitutive model can flexibly reflect the influences of the material microscopic structure via the introduced structural tensor. The observed toe-heel-linear stress-strain relationships and the anisotropic behavior of the tri-layer scaffold material sample demonstrate that it can be used as the scaffold material to mimic the mechanical responses of native heart valve tissues.

Chapter 5

Conclusions and future work

In this chapter, the major conclusions of this thesis are summarized. Then, several potential avenues to further improve the modeling capability of the proposed computational framework are discussed.

5.1 Summary

With the advancement in tissue engineering, tissue-engineered heart valve (TEHV) provides a promising potential to overcome the drawbacks of existing artificial heart valves. With the potential for self-repair, growth, and reduction of long-term complications. TEHVs are designed to integrate into the body's own tissue, gradually adapting to changes in hemodynamic (blood flow) loads over time. However, one of the most significant challenges is to design the scaffold material used in TEHV that closely mimics the mechanical properties of native heart valve tissues. Among various fabrication methods, the electrospinning technology offers an effective approach to fabricate scaffold materials needed in the artificial heart valve.

In order to ensure that the fabricated scaffold material mimics the mechanical properties of native valve tissues, solely relying on experimental trial-and-error is labor-intensive, time-consuming, and financially expensive. On the other hand, numerical methods, especially finite element simulations, provide an efficient approach to investigate the mechanical properties of fabricated scaffold materials. *The main contribution of this thesis is that a computational framework based on the finite element method was developed to model the mechanical responses of the bioinspired tri-layer scaffold used for heart valve constructs.* Specifically, the following tasks were accomplished:

- Based on the experimental observation of the tri-layer scaffold, a hyperelastic constitutive model was appropriately chosen to model the material mechanical behavior. The strain energy function of the constitutive model is composed of three terms, including a volumetric term, an isotropic term, and an anisotropic term. The volumetric strain energy serves as a penalty term to enforce the material incompressibility condition. The isotropic strain energy represents the contribution from the ground matrix material. The anisotropic strain energy represents the contribution from fibers aligned along certain orientations. Particularly, this material model uses the structural tensors to describe the material anisotropy and can accurately describe the material nonlinear behavior. To facilitate the numerical implementation, the detailed expressions of various stress tensors such as the Cauchy stress tensor in the deformed configuration and the 2nd Piola-Kirchhoff (P-K) stress tensor in the reference configuration are presented. The fourth-order material and spatial elasticity tensors are also provided. These expressions can be used to implement the material constitutive model in any finite element packages.

- A three-field mixed finite element procedure was adopted to enforce the material incompressibility and avoid the volumetric locking, which is typically encountered in the numerical modeling of biomaterials. Biomaterials are typically considered as incompressible. At the constitutive model level, this incompressibility constraint can be considered via either a penalty approach or a Lagrange multiplier approach. According to the penalty approach, the material is treated as nearly incompressible, and the volumetric strain energy can be viewed as a penalty term to penalize any material volume change. According to the Lagrange multiplier approach, the material is treated as strictly incompressible, and the pressure field serves as the corresponding Lagrange multiplier to enforce the incompressibility constraint. However, in any finite element simulation of incompressible materials, just enforcing the material incompressibility at the material constitutive model level is insufficient. The finite element spaces need to be carefully selected. Otherwise, the material response would become overly stiff, which is known as the so-called volumetric locking. In this thesis, the well-known three-field mixed formulation is adopted as the finite element approach. This mixed formulation has the advantages of accommodating different combinations of the finite element spaces (or shape functions) for various fields. As a result, the finite element spaces that satisfy the so-called LBB condition (or the inf-sup condition) can be adopted to avoid the volumetric locking. Moreover, detailed expressions of the finite element stiffness matrix and the right-hand side vector are provided to facilitate the development of the finite element implementation.

- The finite element model was created for the tri-layer scaffold material sample. Particularly, the geometry and composition of the honeycomb patterns contained in the middle layer are properly considered, which significantly impact the material anisotropy. The tri-layer biomimetic scaffold sample is composed of three layers with distinctive microscopic structures. The top and bottom layers of the tri-layer sample contain highly aligned fibers that are perpendicular with each other. The middle layer in between contains a series of honeycomb patterns. The microscopic arrangements of the fibers observed via various experimental techniques such as the scanning electron microscope (SEM) imaging and the confocal laser microscope imaging are properly considered in the material constitutive model and the finite element formulation. These fiber arrangements can significantly impact the material nonlinear and anisotropic behaviors.

- The numerical results were compared with the experimental observations to demonstrate the effectiveness and accuracy of the developed computational framework. Each layer of the tri-layer biomimetic scaffold material sample is firstly modeled separately. Then, the entire tri-layer scaffold is modeled as a whole. By comparing with the experimental observations and test data, it is shown that the proposed computational model can not only accurately model the mechanical responses of individual layers but also the nonlinear behavior of the whole scaffold sample. Through these numerical results, it is shown that the geometric arrangement of the honeycomb patterns contained in the middle layer of the scaffold sample can significantly impact the deformation and the stress distributions inside the material. Moreover, from the stress-strain relationships, it can be seen that the fabricated scaffold sample exhibits anisotropic responses under different loading directions. The stress-strain curve can be divided into three distinctive regions, including the toe region, the heel region, and the linear region. These features are consistent with the mechanical response of native biological tissues, demonstrating the validity of the fabricated tri-layer biomimetic sample as the scaffold material for tissue-engineered heart valves.

- Additionally, the computational framework presented in this thesis can be easily adapted to model the mechanical behavior of other biological tissues and bio-inspired materials. At the constitutive model level, a different form of the strain energy function could be adopted, depending on the characteristics of the material system under investigation. The derivation processes of various stress measures and elasticity tensors are the same, involving the chain rules of the partial derivatives. On the other hand, the presented three-field mixed finite element formulation is a general technique used to enforce the material incompressibility. The mixed formulation can be

easily adapted to model the mechanical behavior of other incompressible biomaterials.

The work related to this thesis is published in a peer-reviewed journal paper [60].

5.2 Future work

There are at least three avenues to further improve the capability of the proposed computational framework:

- Currently, the fabricated tri-layer biomimetic scaffold material is considered within the framework of hyperelasticity. Based on this assumption, the corresponding hyperelastic strain energy function is constructed, and the stress tensor and the elasticity tensor are derived. However, in reality, the scaffold material might exhibit viscoelastic responses under long-term loading conditions. Therefore, the proposed computational framework needs to be expanded to consider the material viscoelasticity.

- In this thesis, the developed material constitutive model only incorporates the global impact of the fibers in a collective manner, that is, the mechanical responses of the fibers are reflected via the directional vectors and several phenomenological parameters. This modeling approach can effectively capture the material macroscopic responses, but is unable to reveal the impact of fiber-level stresses on the material global behavior. One option is to adopt the multiscale modeling approach that incorporates the material microstructures into the finite element simulations. This option could more comprehensively reveal the material structure-function relationship.

- The tri-layer material sample is designed as the scaffold material for tissue-engineered heart valves. For this purpose, multiple cells need to be embedded into the scaffold material for tissue growth and remodeling. Currently, the thesis mainly focuses on the mechanical responses of the scaffold material sample. Eventually, the presence of cells needs also to be incorporated into the finite element simulations to investigate the cell alignment and proliferation behavior.

- Lastly, the developed computational framework for the tri-layer scaffold material will be used in the full heart valve modeling, which typically involves the effect of the fluid-structure interactions.

The above avenues will be further explored in the future research.

References

[1] M H Yacoub and J J M Takkenberg. Will heart valve tissue engineering change the world? *Nature Clinical Practice Cardiovascular Medicine*, 2(2):60–61, 2005.

[2] R Brandt and Philippe Pibarot. Prosthetic heart valves: Part 1–selection. *e-Journal of Cardiology Practice [Internet]*, 20(1), 2021.

[3] Mahmoud Sesa, Hagen Holthusen, Lukas Lamm, Christian Böhm, Tim Brepols, Stefan Jockenhövel, and Stefanie Reese. Mechanical modeling of the maturation process for tissue-engineered implants: Application to biohybrid heart valves. *Computers in Biology and Medicine*, 167:107623, 2023.

[4] Hossein Ghanbari, Helene Viatge, Asmeret G Kidane, Gaetano Burriesci, Mehdi Tavakoli, and Alexander M Seifalian. Polymeric heart valves: new materials, emerging hopes. *Trends in biotechnology*, 27(6):359–367, 2009.

[5] Mary Jialu Chen, Georgios A Pappas, Daniele Massella, Arthur Schlothauer, Sarah E Motta, Volkmar Falk, Nikola Cesarovic, and Paolo Ermanni. Tailoring crystallinity for hemocompatible and durable peek cardiovascular implants. *Biomaterials advances*, 146:213288, 2023.

[6] Richard L Li, Jonathan Russ, Costas Paschalides, Giovanni Ferrari, Haim Waisman, Jeffrey W Kysar, and David Kalfa. Mechanical considerations for polymeric heart valve development: Biomechanics, materials, design and manufacturing. *Biomaterials*, 225:119493, 2019.

[7] T C Flanagan and A Pandit. Living artificial heart valve alternatives: A review. *European Cells and Materials*, 6:28–45, 2003.

[8] Christopher A Durst, Michael P Cuchiara, Elizabeth G Mansfield, Jennifer L West, and K Jane Grande-Allen. Flexural characterization of cell encapsulated PEGDA

hydrogels with applications for tissue engineered heart valves. *Acta biomaterialia*, 7(6):2467–2476, 2011.

[9] Maximilian Y Emmert and Simon P Hoerstrup. Tissue engineered heart valves: moving towards clinical translation. *Expert review of medical devices*, 13(5):417–419, 2016.

[10] Dimosthenis Mavrilas and Yannis Missirlis. An approach to the optimization of preparation of bioprosthetic heart valves. *Journal of Biomechanics*, 24(5):331–339, 1991.

[11] Richard L. Li, Jonathan Russ, Costas Paschalides, Giovanni Ferrari, Haim Waisman, Jeffrey W. Kysar, and David Kalfa. Mechanical considerations for polymeric heart valve development: Biomechanics, materials, design and manufacturing. *Biomaterials*, 225:119493, 2019.

[12] Anwarul Hasan, Kim Ragaert, Wojciech Swieszkowski, Šeila Selimović, Arghya Paul, Gulden Camci-Unal, Mohammad RK Mofrad, and Ali Khademhosseini. Biomechanical properties of native and tissue engineered heart valve constructs. *Journal of biomechanics*, 47(9):1949–1963, 2014.

[13] Niels JB Driessen, Anita Mol, Carlijn VC Bouten, and Frank PT Baaijens. Modeling the mechanics of tissue-engineered human heart valve leaflets. *Journal of biomechanics*, 40(2):325–334, 2007.

[14] Sandra Loerakker, Giulia Argento, Cees WJ Oomens, and Frank PT Baaijens. Effects of valve geometry and tissue anisotropy on the radial stretch and coaptation area of tissue-engineered heart valves. *Journal of biomechanics*, 46(11):1792–1800, 2013.

[15] Jay D Humphrey and Rajagopal. A constrained mixture model for growth and remodeling of soft tissues. *Mathematical models and methods in applied sciences*, 12(03):407–430, 2002.

[16] T Christian Gasser, Ray W Ogden, and Gerhard A Holzapfel. Hyperelastic modelling of arterial layers with distributed collagen fibre orientations. *Journal of the royal society interface*, 3(6):15–35, 2006.

[17] Maximilian Y Emmert, Boris A Schmitt, Sandra Loerakker, Bart Sanders, Hendrik Spriestersbach, Emanuela S Fioretta, Leon Bruder, Kerstin Brakmann, Sarah E Motta, Valentina Lintas, et al. Computational modeling guides tissue-engineered heart valve design for long-term in vivo performance in a translational sheep model. *Science translational medicine*, 10(440):eaan4587, 2018.

[18] Pin Tong and Yuang-Cheng Fung. The stress-strain relationship for the skin. *Journal of biomechanics*, 9(10):649–657, 1976.

[19] YC Fung, K Fronek, and P Patitucci. Pseudoelasticity of arteries and the choice of its mathematical expression. *American Journal of Physiology-Heart and Circulatory Physiology*, 237(5):H620–H631, 1979.

[20] CJ Chuong and YC Fung. Three-dimensional stress distribution in arteries. 1983.

[21] Tao Jin, Aya Chams, and Xing Zhang. Impact of mathematical requirements on the invariant-based anisotropic constitutive models for non-linear biomaterials. *International Journal of Non-Linear Mechanics*, 147:104188, 2022.

[22] Y Lanir. A structural theory for the homogeneous biaxial stress-strain relationships in flat collagenous tissues. *Journal of biomechanics*, 12(6):423–436, 1979.

[23] Shruti Motiwale and Michael S Sacks. Structural constitutive models for soft biological tissues and biomaterials: the role of mechanical interactions. *Mechanics of Soft Materials*, 7(1):1–39, 2025.

[24] Tao Jin and Ilinca Stanciulescu. Numerical simulation of fibrous biomaterials with randomly distributed fiber network structure. *Biomechanics and Modeling in Mechanobiology*, 15:817–830, 2016.

[25] Tao Jin. A computational framework for biomaterials containing three-dimensional random fiber networks based on the affine kinematics. *Biomechanics and Modeling in Mechanobiology*, 21:685–708, 2022.

[26] Tao Jin and Ilinca Stanciulescu. Numerical investigation of the influence of pattern topology on the mechanical behavior of pegda hydrogels. *Acta Biomaterialia*, 49:247–259, 2017.

[27] Qian Li, Yun Bai, Tao Jin, Shuo Wang, Wei Cui, Ilinca Stanciulescu, Rui Yang, Hemin Nie, Linshan Wang, and Xing Zhang. Bioinspired engineering of poly(ethylene glycol) hydrogels and natural protein fibers for layered heart valve constructs. *ACS Applied Materials & Interfaces*, 9(19):16524–16535, 2017. PMID: 28448124.

[28] Tao Jin and Ilinca Stanciulescu. Computational modeling of the arterial wall based on layer-specific histological data. *Biomechanics and Modeling in Mechanobiology*, 15:1479–1494, 2016.

[29] Trenton Kirchdoerfer and Michael Ortiz. Data-driven computational mechanics. *Computer Methods in Applied Mechanics and Engineering*, 304:81–101, 2016.

[30] Jamshid Ghaboussi, JH Garrett Jr, and Xiping Wu. Knowledge-based modeling of material behavior with neural networks. *Journal of engineering mechanics*, 117(1):132–153, 1991.

[31] Marek Lefik and Bernhard A Schrefler. Artificial neural network as an incremental non-linear constitutive model for a finite element code. *Computer methods in applied mechanics and engineering*, 192(28-30):3265–3283, 2003.

[32] Theodore Sussman and Klaus-Jürgen Bathe. A model of incompressible isotropic hyperelastic material behavior using spline interpolations of tension–compression test data. *Communications in numerical methods in engineering*, 25(1):53–63, 2009.

[33] Gerhard A Holzapfel and Ray W Ogden. Constitutive modelling of arteries. *Proceedings of the Royal Society A: Mathematical, Physical and Engineering Sciences*, 466(2118):1551–1597, 2010.

[34] Alp Kağan Açan, Oğuz Ziya Tikenoğullari, and Hüsnü Dal. A data-driven constitutive model for soft biological tissues. *PAMM*, 23(4):e202300239, 2023.

[35] Gerhard A Holzapfel, Thomas C Gasser, and Ray W Ogden. A new constitutive framework for arterial wall mechanics and a comparative study of material models. *Journal of elasticity and the physical science of solids*, 61:1–48, 2000.

[36] Wei Sun, Ajay Abad, and Michael S Sacks. Simulated bioprosthetic heart valve deformation under quasi-static loading. 2005.

[37] Mostafa Abbasi, Mohammed S Barakat, Koohyar Vahidkhah, and Ali N Azadani. Characterization of three-dimensional anisotropic heart valve tissue mechanical properties using inverse finite element analysis. *Journal of the mechanical behavior of biomedical materials*, 62:33–44, 2016.

[38] Anvar Gilmanov, Henryk Stolarski, and Fotis Sotiropoulos. Non-linear rotation-free shell finite-element models for aortic heart valves. *Journal of biomechanics*, 50:56–62, 2017.

[39] Aditya Balu, Sahiti Nallagonda, Fei Xu, Adarsh Krishnamurthy, Ming-Chen Hsu, and Soumik Sarkar. A deep learning framework for design and analysis of surgical bioprosthetic heart valves. *Scientific reports*, 9(1):18560, 2019.

[40] Devin W Laurence, Patricia M Sabin, Analise M Sulentic, Matthew Daemer, Steve A Maas, Jeffrey A Weiss, and Matthew A Jolley. Febio finesse: An open-source finite element simulation approach to estimate in vivo heart valve strains using shape enforcement. *Annals of Biomedical Engineering*, pages 1–19, 2024.

[41] Afshin Anssari-Benam, Andrea Bucchi, Hazel RC Screen, and Sam L Evans. A transverse isotropic viscoelastic constitutive model for aortic valve tissue. *Royal Society Open Science*, 4(1):160585, 2017.

[42] Will Zhang, Salma Ayoub, Jun Liao, and Michael S Sacks. A meso-scale layer-specific structural constitutive model of the mitral heart valve leaflets. *Acta biomaterialia*, 32:238–255, 2016.

[43] Javier Bonet and Richard D. Wood. *Nonlinear Continuum Mechanics for Finite Element Analysis*. Cambridge University Press, 2 edition, 2008.

[44] Daniel Arndt, Wolfgang Bangerth, Marco Feder, Marc Fehling, Rene Gassmöller, Timo Heister, Luca Heltai, Martin Kronbichler, Matthias Maier, Peter Munch, Jean-Paul Pelteret, Simon Sticko, Bruno Turcksin, and David Wells. The `deal.II` library, version 9.4. *Journal of Numerical Mathematics*, 30(3):231–246, 2022.

[45] Carlo Sansour. On the physical assumptions underlying the volumetric-isochoric split and the case of anisotropy. *European Journal of Mechanics - A/Solids*, 27(1):28–39, 2008.

[46] J. Helfenstein, M. Jabareen, E. Mazza, and S. Govindjee. On non-physical response in models for fiber-reinforced hyperelastic materials. *International Journal of Solids and Structures*, 47(16):2056–2061, 2010.

[47] Tao Jin and Ilinca Stanciulescu. A note on the volumetric-deviatoric split on the anisotropic constitutive model for fiber-reinforced materials. *Biomedical Engineering International*, 1(4):16–24, 2019.

[48] J.C. Simo, R.L. Taylor, and K.S. Pister. Variational and projection methods for the volume constraint in finite deformation elasto-plasticity. *Computer Methods in Applied Mechanics and Engineering*, 51(1):177–208, 1985.

[49] Juan C. Simo and Robert L. Taylor. Quasi-incompressible finite elasticity in principal stretches. continuum basis and numerical algorithms. *Computer Methods in Applied Mechanics and Engineering*, 85(3):273–310, 1991.

[50] Hai-Chang Hu. On some variational principles in the theory of elasticity and the theory of plasticity. *Acta Physica Sinica*, 10:259–290, 1954.

[51] K. Washizu. On the variational principles of elasticity and plasticity. Technical report, Massachusetts Inst of Tech Cambridge Aeroelastic and Structures Research Lab, 1955.

[52] Gerhard A. Holzapfel. *Nonlinear Solid Mechanics: A Continuum Approach for Engineering*. John Wiley & Sons., 2000.

[53] Ivo Babuška. The finite element method with lagrangian multipliers. *Numerische Mathematik*, 20:179–192, 1973.

[54] F. Brezzi. On the existence, uniqueness and approximation of saddle-point problems arising from lagrangian multipliers. *Revue française d'automatique, informatique, recherche opérationnelle. Analyse numérique*, 8(R2):129–151, 1974.

[55] Thomas J. R. Hughes. *The Finite Element Method: Linear Static and Dynamic Finite Element Analysis*. Dover, 2000.

[56] K Misof, G Rapp, and P Fratzl. A new molecular model for collagen elasticity based on synchrotron X-ray scattering evidence. *Biophysical Journal*, 72(3):1376–1381, 1997.

[57] B A Roeder, K Kokini, J E Sturgis, J P Robinson, and S L Voytik-Harbin. Tensile mechanical properties of three-dimensional type I collagen extracellular matrices with varied microstructure. *Journal of Biomechanical Engineering*, 124(2):214–222, 2002.

[58] Lijuan Zhang, Spencer P Lake, Victor K Lai, Catalin R Picu, Victor H Barocas, and Mark S Shephard. A coupled fiber-matrix model demonstrates highly inhomogeneous microstructural interactions in soft tissues under tensile load. *Journal of Biomechanical Engineering*, 135(1):011008(1)–011008(9), 2013.

[59] A Hasan, K Ragaert, W Swieszkowski, T Selimović, A Paul, G Camci-Unal, M R K Mofrad, and A Khademhosseini. Biomechanical properties of native and tissue engineered heart valve constructs. *Journal of Biomechanics*, 47(9):1949–1963, 2014.

[60] Zeping Zhang, Rizheng Han, Yueen Liu, Xinqi Yu, Guixue Wang, Yun Bai, Rui Yang, Tao Jin, and Xing Zhang. Bioinspired trilayer poly(ϵ-caprolactone) scaffolds with native-like structures and mechanical property for heart valve constructs. *Chemical Engineering Journal*, 518:164550, 2025.